*sustainability*

MDPI

*Article*

# Integrating Multi-Temporal Sentinel-1 InSAR, GIS-Based Susceptibility Modeling, and Geotechnical Monitoring for Sustainable Dam Safety: Capabilities and Limits at the Yaprak Dam Reservoir, Türkiye

**Tuğrul Urfalı [1,*] and Furkan Karlıtepe [2]**

[1] Department of Architecture and Urban Planning, Tokat Vocational School, Tokat Gaziosmanpaşa University, Tokat 60250, Türkiye
[2] Department of Geomatics Engineering, Faculty of Engineering and Architecture, Tokat Gaziosmanpaşa University, Tokat 60250, Türkiye; karlitepefurkan@gmail.com
* Correspondence: tugrulurfali@gmail.com

**Abstract**

Reservoir slope instability threatens the safe and sustainable operation of dams. This study tests what open access data can reveal about a reactivated landslide on the left-bank reservoir slope of the Yaprak I Dam (Amasya, Türkiye) by combining multi-temporal Sentinel-1 InSAR, SAR-derived reservoir surface area, a GIS-based weighted overlay susceptibility model, and site-investigation data. Ascending and descending 2017–2024 interferograms were inverted with a small-baseline approach and decomposed into vertical and east–west components. In the instrumented sector, mean line-of-sight velocities ranged from −1.1 to +1.6 mm/yr and the east–west component was about −2 mm/yr, all below the local detection threshold of about 5 mm/yr ($2\sigma$). This agrees with the 2.8–7.9 mm recorded by six inclinometers over 4–12 months in 2022–2023, whereas the 20.6–24.9 mm recorded by two older casings in July–November 2022 were not resolved. Correlations between reservoir surface area and displacement were not significant after correction for multiple testing, and InSAR anomalies were distributed among susceptibility classes in proportion to their area, irrespective of the factor weights. Open access InSAR thus bounds east–west and vertical slope motion at a few millimetres per year at low cost, but is insensitive to north–south and small-scale movements and cannot replace in situ monitoring.

**Keywords:** sustainable infrastructure management; dam safety; reservoir landslide; multi-temporal InSAR; Sentinel-1; landslide susceptibility; inclinometer; MASW

Check for updates

Academic Editor: George D. Bathrellos

Received: 5 October 2026
Revised: 24 October 2026
Accepted: 26 October 2026
Published: 28 October 2026

**Copyright:** © 2026 by the authors. Licensee MDPI, Basel, Switzerland. This article is an open access article distributed under the terms and conditions of the Creative Commons Attribution (CC BY) license.

## 1. Introduction

Dams are critical components of modern infrastructure due to their strategic roles in hydroelectric power generation, irrigation water supply, and flood control. However, these large engineering structures are continuously exposed to deformation risks driven by reservoir water load variations, ground settlement, seismic activity, and the long-term degradation of geological units. The interaction between hydrological cycles and geotechnical responses increases the complexity of deformation processes affecting dam bodies and reservoir slopes [1]. The early detection of millimetric movements is therefore essential to reduce the potential consequences of dam failure, which may result in severe loss of life and property [2,3].

Ensuring the long-term safety of dams is also a sustainability issue. Reservoirs underpin water supply, irrigation and renewable hydropower generation, and slope failures along reservoir margins can damage infrastructure, reduce storage capacity and endanger nearby settlements. Monitoring approaches that rely on freely available satellite data and on information already collected during routine site investigations can make continuous safety assessment more affordable, thereby supporting resource-efficient and risk-informed management of water infrastructure over its service life.

Inclinometer measurements are widely regarded as a reference method for monitoring slope instabilities, as they enable the detection of subsurface deformations, identification of active shear zones, and determination of movement depths [4]. By capturing the internal kinematics of unstable masses, inclinometers provide valuable insight into deformation that is not observable at the surface. However, their discrete measurements, high installation costs, and limited spatial coverage limit their ability to represent deformation over large dam bodies and reservoir slopes. As a result, dam safety assessments that rely on periodic inspections and localized geotechnical measurements often lack the spatial continuity and temporal resolution required for the early detection of subtle deformation [5]. To address these limitations, satellite-based remote sensing technologies, such as Interferometric Synthetic Aperture Radar (InSAR), have become established tools for deformation monitoring. InSAR enables surveillance of surface deformation over wide geographic areas with millimetric precision [6–8]. InSAR provides surface deformation affecting dams and their surrounding slopes without the need for dense ground-based instrumentation [9–12]. Previous studies have shown good agreement between InSAR-derived deformation and ground-based observations at hydraulic structures [11,12]. Despite these advances, deformation rates alone are insufficient for effective risk assessment. Understanding the mechanisms and triggering factors controlling slope movements remains equally important. Numerous studies have shown that rapid reservoir water level variations, particularly drawdown effects, can alter pore water pressure conditions and adversely affect slope stability [13–15]. The integration of satellite-based interferometry and in situ geotechnical measurements enables continuous monitoring of subtle deformation linked to reservoir water level fluctuations [7,16]. However, many existing investigations still treat surface deformation, environmental factors such as slope, Topographic Wetness Index (TWI), and land use, and subsurface mechanical properties independently, limiting the ability to fully resolve deformation [17].

In this context, the integration of satellite-based observations with geotechnical and geophysical methods has been recognized as a key requirement for understanding slope instability processes and for supporting early warning systems [18,19]. Such comprehensive monitoring approaches are relevant for identifying short-term precursors to potential failures and improving the forecasting of both natural and anthropogenic hazards associated with dam operations [20]. The combined use of InSAR with ground-based monitoring techniques such as inclinometers and Multichannel Analysis of Surface Waves (MASW) provides a basis for validating satellite-derived deformation signals and for characterizing subsurface conditions that influence slope stability [7,21].

Most InSAR studies of dams focus on the deformation of the dam body itself or on comparisons between InSAR and geodetic measurements [9,12,16,22,23], whereas studies that combine InSAR with susceptibility mapping usually work at regional scale [17,19]. The contribution of the present study is therefore not a new processing algorithm but a site-scale integration workflow for a reactivated landslide on a reservoir slope, in which open access Sentinel-1 data are interpreted together with data that were already available from the site investigation of the slope (MASW, electrical resistivity tomography and inclinometers). The study tests three hypotheses, each with a quantitative indicator:

**H1.** *The instrumented sector of the slope moved at a rate that can be resolved by Sentinel-1 InSAR,* i.e., *its mean velocity exceeds twice the local velocity noise (indicators: line-of-sight (LOS), vertical and east–west velocities for 2017–2024 and for the inclinometer period 2022–2023, compared with the noise level and with the inclinometer displacements).*

**H2.** *The displacement of the slope varies with the reservoir level (indicator: correlation coefficient and time lag between SAR-derived reservoir surface area and InSAR displacement).*

**H3.** *InSAR-detected deformation occurs more frequently in the higher classes of a geographic information system (GIS)-based susceptibility model than expected from their areal extent (indicator: frequency ratio of InSAR anomalies per susceptibility class).*

The InSAR results are interpreted together with the subsurface information provided by MASW, resistivity and inclinometer data. The contribution of the study is therefore twofold: it quantifies, for a reservoir slope with independent in situ observations, the detection threshold and directional sensitivity of open access InSAR, and it tests an expert-weighted susceptibility map statistically against the InSAR results, including a sensitivity analysis of the weights; both steps are often omitted when such data are used for screening. By relying mainly on freely available satellite data and on routine investigation data, the workflow is intended as a low-cost screening tool that can support the sustainable management of dam reservoirs.

## 2. Materials and Methods

This section provides a description of the methodologies employed in this study, encompassing the acquisition and processing of satellite imagery for InSAR analysis, the development of a GIS-based landslide susceptibility model, and the application of geophysical and geotechnical techniques. The following subsections describe the datasets, parameters, and analytical procedures adopted within each methodological component, emphasizing their individual roles and their combined contribution to deformation analysis. This multidisciplinary study facilitates cross-validation among independent data sources, thereby reducing the methodological limitations and improving the reliability and interpretability of the results [24]. Moreover, such integrated monitoring strategies support the identification of deformation features that may not be detectable through individual approaches alone, which is particularly important for risk assessment in hydropower infrastructures [25]. Within this approach, InSAR plays a key role by enabling the remote evaluation of displacement fields and temporal deformation associated with hydrometeorological, geological, and anthropogenic influences, complementing localized but high-resolution geotechnical observations [22].

Figure 1 illustrates an overview of the integrated workflow applied at the Yaprak Dam. The methodology is structured into three interconnected phases. Phase 1, Data Acquisition and Inputs, includes the collection of Sentinel-1 SAR imagery, Sentinel-2 optical data, Shuttle Radar Topography Mission (SRTM) digital elevation models, geological maps, and in situ measurements obtained from inclinometer installations and MASW surveys. These datasets form the basis for Phase 2, Analysis, which is subdivided into three parallel and interacting components. The Remote Sensing Analysis involves a small-baseline time-series analysis of ascending and descending Sentinel-1 interferograms to derive LOS velocity maps, time series and vertical and east–west velocity components, together with the extraction of reservoir surface-area variations from radar backscatter information. In parallel, the GIS-based susceptibility modeling generates multiple conditioning factor layers, including slope, aspect, Topographic Wetness Index, and fault distance, which are subsequently

reclassified, weighted, and combined using the Weighted Overlay Method to produce a final landslide susceptibility map. At the same time, the geotechnical and geophysical analysis component evaluates cumulative displacement profiles from inclinometer measurements and shear-wave velocity ($V_s$) structures derived from MASW surveys, allowing subsurface deformation characteristics to be constrained. Phase 3, Integration and Hypothesis Testing, brings together the outputs of these analytical components to test Hypotheses H1–H3 (Section 1) [5,7,23].

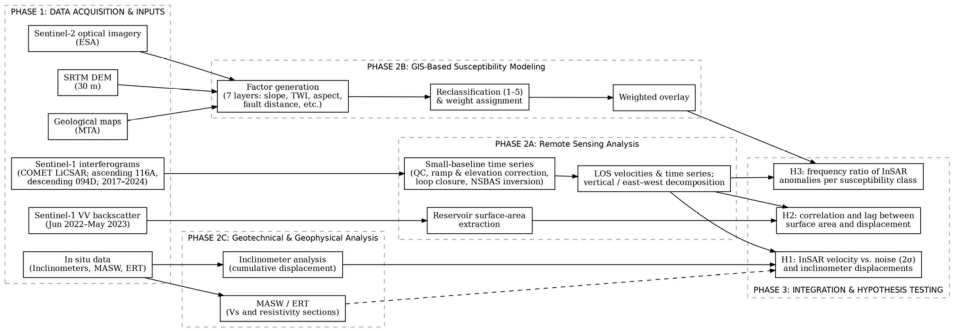



**Figure 1.** Methodological workflow of the study: data acquisition, multi-processing stages, and validation phases. Solid boxes denote data sets and processing steps, and dashed frames group them into phases; solid arrows show the flow of data and results, and the dashed arrow indicates that the MASW and ERT sections were used only as supporting information in the interpretation of H1.

### *2.1. Study Area*

The study area is the left-bank slope of the reservoir of the Yaprak I Dam, which forms part of the Yaprak I Dam and Hydroelectric Power Plant (HPP) project in Taşova district, Amasya Province, Türkiye. The project area lies approximately 48 km northwest of the Taşova town centre and approximately 3 km northeast of Kavaloluğu village, on the 1:25,000-scale Tokat G36-b1 map sheet. Constructed as a clay-core earthfill structure, the dam is part of a dam and hydroelectric power plant project. The region exhibits a continental climate characterized by marked seasonal temperature fluctuations, freeze–thaw cycles, and irregular precipitation patterns, which constitute environmental factors influencing soil behavior and slope stability.

According to the site investigation report of the landslide, the slope is underlain by an Upper Cretaceous flysch sequence of sandstone, claystone, mudstone and marl alternations, locally cut by andesitic–basaltic dykes and overlain by a debris cover containing clay and blocks; the uppermost 0.5–1.0 m consists of clayey agricultural soil. Borehole, resistivity and seismic results from the same investigation describe weathered phyllite and sandy–silty–clayey soils in the upper levels and massive to moderately hard phyllite at depth. The site lies in the highest seismic hazard zone of the former Turkish earthquake zoning map, 5–15 km from the Erbaa–Alparslan–Destek–Ladik branch of the North Anatolian Fault. The same report interprets the landslide as the reactivation of an older landslide mass after reservoir impoundment and notes several seepage springs around the landslide, which indicate groundwater movement within the slope. Two inclinometers were installed on the slope in 2020 and monitored between April and July 2020; following reports of renewed movement in 2022, a site investigation was carried out in November 2022 that comprised 30 m deep boreholes, six new inclinometer casings, five electrical resistivity tomography (ERT) profiles and five two-dimensional MASW lines. Accordingly, the study area encompasses the dam body, reservoir slopes, and adjacent zones wherein deformation has been identified.

The spatial extent of the study area, together with the locations of inclinometer boreholes employed for subsurface deformation monitoring and the approximate positions of the MASW lines and ERT profiles, is illustrated in Figure 2. This spatial configuration

provides the foundation for the integrated analysis of surface deformation, subsurface conditions, and environmental controls addressed in the subsequent sections.

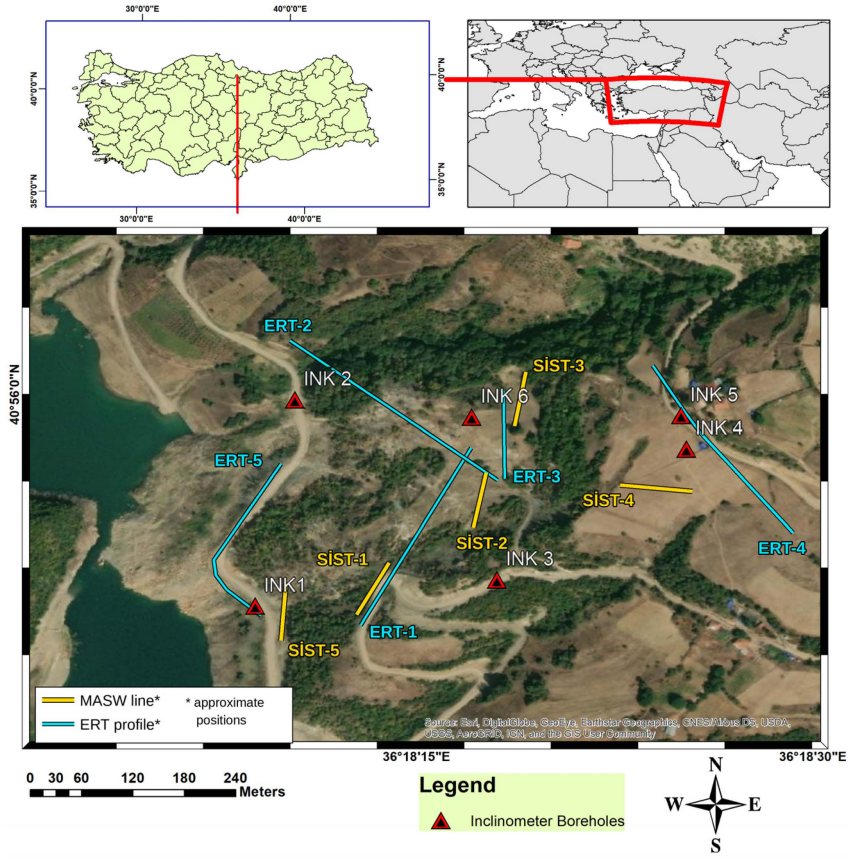



**Figure 2.** Location of the Yaprak Dam study area and distribution of inclinometer boreholes (INK1–INK6), MASW lines (SİST-1 to SİST-5) and ERT profiles (ERT-1 to ERT-5). The positions of the MASW lines and ERT profiles were transferred from the location sketch of the site investigation report and are approximate (Section 2.4). In the legend, these approximate positions are marked with an asterisk (*).

### *2.2. Datasets*

A multisource dataset integrating remote sensing products, geophysical measurements, and in situ geotechnical observations was compiled to analyze slope instability processes at the Yaprak Dam site (Table 1). The primary remote sensing dataset comprised Sentinel-1 C-band SAR data, used for a multi-temporal (small-baseline) InSAR analysis of surface deformation and to monitor reservoir surface-area variations. Complementary optical imagery from Sentinel-2 was employed to compute the Normalized Difference Vegetation Index (NDVI), and land use was taken from the ESA WorldCover 10 m land cover product, version 200, which represents the year 2021 (Section 2.5). The NDVI was computed from bands B8 and B4 of a median composite of the Sentinel-2 Level-2A (surface reflectance, harmonized collection) images acquired between June and August 2024 with less than 20% cloud cover, a period chosen to represent the peak of the growing season, processed in Google Earth Engine and exported at 10 m. Topographic parameters were derived from the 30 m resolution SRTM Digital Elevation Model (DEM). The TWI was computed in Google Earth Engine as $\ln(A/\tan \beta)$, where $\beta$ is the slope derived from the SRTM DEM and A is the flow accumulation (number of upstream cells) of the HydroSHEDS product at 15 arc-seconds (approximately 450 m), and was exported at 30 m. Fault traces were taken from the digital active fault database of the General Directorate of Mineral Research and

Exploration (MTA; 2013 version), which is compiled on 1:25,000-scale map sheets. The MASW, ERT, borehole and inclinometer data were obtained from the reports of the site investigation and monitoring of the landslide described in Section 2.1, which were made available to the authors for this study.

**Table 1.** Datasets used in this study.

| Data Type | Source/Sensor | Resolution/Scale | Period | Purpose |
|---|---|---|---|---|
| SAR interferograms | Sentinel-1A, processed by COMET LiCSAR | C-band; multilooked to 0.001° (approx. 100 m) | January 2017–December 2024 (ascending and descending) | Surface deformation time series |
| SAR backscatter | Sentinel-1 (ESA) | C-band, VV | June 2022–May 2023 | Reservoir surface area |
| Optical imagery | Sentinel-2 (ESA) | 10 m | June–August 2024 (median composite) | NDVI |
| Land cover | ESA WorldCover | 10 m | 2021 (version 200) | Land use factor |
| DEM | SRTM | 30 m | 2000 | Slope, aspect, elevation, TWI |
| Active fault data | MTA | 1:25,000 | 2013 version | Distance to faults |
| Geophysical data | Five 2D MASW lines and five ERT profiles | 2D profiles | November 2022 | Shear-wave velocity and resistivity structure |
| Boreholes | Site investigation | 30 m depth | November 2022 | Lithology and casing installation |
| In situ data | Inclinometers INK1–INK6 | 0.5 m reading interval | November 2022–2023 | Subsurface displacement |

The conditioning factor layers of the susceptibility model were processed in geographic coordinates (WGS 84, EPSG:4326) and combined on a common grid with a cell size of 0.000315° (approximately 27 m × 35 m). Following the default settings of the weighted overlay tool (ArcGIS Spatial Analyst, ArcGIS Desktop 10.4; Esri, Redlands, CA, USA), the output grid adopted the coarsest input resolution, that of the 30 m distance-to-faults raster, and the finer layers (10 m land use and NDVI layers and the 30 m topographic layers) were resampled to it internally by nearest-neighbour assignment. The InSAR products have a pixel spacing of 0.001° (approximately 84 m × 111 m). Because the datasets differ in spatial resolution (from 10 m optical pixels to 1:25,000-scale fault data and point-like inclinometers) and in acquisition period, the comparison between InSAR and the susceptibility map is made at the InSAR pixel scale, and the comparison with the inclinometers at the scale of the instrumented slope sector. The acquisition periods of the main datasets are given in Table 1.

### *2.3. Multi-Temporal InSAR Processing and Reservoir Surface Area Extraction*

Multi-temporal InSAR combines the phase of many interferograms of the same area to estimate time-dependent surface displacements. The interferometric phase $\phi_{int}$ at pixel $x$ in the $i$-th interferogram can be modeled as the sum of several components [26]:

$$\phi_{int}(x,i) = \phi_{def}(x,i) + \phi_{atm}(x,i) + \phi_{orb}(x,i) + \phi_{noise}(x,i) \quad (1)$$

where $\phi_{def}(x,i)$ represents the phase change due to deformation along the satellite's LOS direction. This is the signal of interest for displacement measurements. The fundamental

relationship between the interferometric phase change and the displacement along the LOS direction is given by [27,28]:

$$\phi_{def} = -\frac{4\pi}{\lambda} d \quad (2)$$

where $\lambda$ is the radar wavelength and $d$ is the displacement in the LOS direction. The term $\phi_{atm}(x,i)$ accounts for the atmospheric phase delay, which is caused by variations in the refractive index of the atmosphere due to changes in temperature, pressure, and water vapor content [29,30]. The term $\phi_{orb}(x,i)$ represents the residual orbital phase errors, and $\phi_{noise}(x,i)$ encompasses residual noise from various sources, including instrument noise, decorrelation, co-registration errors, and inaccuracies in the Digital Elevation Model.

Interferograms were obtained from the COMET LiCSAR system (University of Leeds, Leeds, UK) [31], which provides geocoded, multilooked (approximately 100 m), filtered and unwrapped Sentinel-1 interferograms and coherence maps for predefined frames. Two frames cover the study area, one in ascending and one in descending geometry (Table 2). For each frame, all interferograms between Sentinel-1A acquisitions with temporal baselines of 12–48 days from January 2017 to December 2024 were clipped to a window of 0.40° × 0.20° around the dam (36.10–36.50° E, 40.83–41.03° N). The time-series analysis followed the main steps of the LiCSBAS package [32], but the package itself was not used; the processing was implemented by the authors in Python 3 (with the NumPy and SciPy libraries): (i) interferograms with an unwrapped coverage below 30% or a mean coherence below 0.10 within the 0.15° × 0.09° analysis area (36.22–36.37° E, 40.89–40.98° N) were discarded; (ii) for each interferogram, an offset, a planar ramp and a linear phase–elevation term [33] were estimated by iterative least squares on coherent pixels (coherence ≥ 0.4) outside a 0.08° × 0.05° box that contains the landslide, and removed from the whole interferogram, which reduces orbital ramps and stratified tropospheric delays and refers all displacements to the surrounding area; (iii) interferograms that occurred only in loops with a root-mean-square closure error above 1.5 rad were discarded; (iv) the displacement time series was estimated pixel by pixel with a small-baseline least-squares inversion [34] in the NSBAS formulation [35], in which a weak linear-in-time constraint (weight $\gamma = 10^{-4}$) connects parts of the network that are separated by gaps; and (v) a linear trend and an annual sinusoid were fitted to each time series, both for the whole period (2017–2024) and for the period 2022–2023, which covers the inclinometer measurements. Pixels with a mean coherence below 0.10 or an inversion residual above 1.5 rad were masked. Tropospheric corrections based on the Generic Atmospheric Correction Online Service (GACOS) are provided by LiCSAR for only part of the epochs (e.g., 19 of 60 ascending and 39 of 60 descending epochs in 2022–2023) and were therefore not applied. The processing parameters are summarized in Table 2.

The velocity noise was characterized empirically as the standard deviation $\sigma_v$ of the velocities of all valid pixels in a 0.08° × 0.06° area around the instrumented sector, excluding a 0.02° × 0.016° box that contains the sector (about 4300 pixels); velocities with an absolute value larger than $2\sigma_v$ (approximately 5 mm/yr, Table 2) are considered significant. This empirical value is larger than the formal velocity uncertainties of the least-squares fit (about 0.1 mm/yr), which neglect temporally correlated noise. Positive LOS values indicate motion towards the satellite. Because the two geometries observe the ground from opposite sides, the ascending and descending velocities were combined to estimate the vertical ($d_U$) and east–west ($d_E$) components:

$$d_{LOS} = e_E d_E + e_N d_N + e_U d_U \quad (3)$$

where $e_E$, $e_N$ and $e_U$ are the components of the LOS unit vector (Table 2). The north component $d_N$, to which both geometries are only weakly sensitive ($|e_N| \approx 0.1$), was neglected, and the resulting 2 × 2 system was solved at each pixel after nearest-neighbour resampling of

the descending grid onto the ascending grid (offset below 0.25 pixel). Consequently, north–south motion is poorly resolved. The instrumented sector is defined as an approximately 0.8 km$^2$ polygon that encloses inclinometers INK1–INK6 (Figure 3); its mean velocities and its mean displacement time series were computed from the valid pixels inside the polygon.

**Table 2.** Sentinel-1 InSAR data and time-series processing parameters.

| Parameter | Ascending | Descending |
|---|---|---|
| LiCSAR frame | 116A_04978_131311 | 094D_04913_101213 |
| Satellite, mode, polarization | Sentinel-1A, IW, VV | Sentinel-1A, IW, VV |
| First and last epoch | 6 January 2017–1 November 2024 | 5 January 2017–30 December 2024 |
| Interferograms available/used | 644/468 | 639/440 |
| Epochs used | 230 | 224 |
| Temporal baselines | 12–48 days | 12–48 days |
| Network gaps bridged by the NSBAS constraint | 5 | 8 |
| Mean incidence angle | 33.4° | 37.5° |
| LOS unit vector (east, north, up) | (−0.54, −0.10, 0.83) | (0.60, −0.11, 0.79) |
| Pixel spacing | 0.001° | 0.001° |
| Valid pixels in the analysis area | 11,962 of 13,500 | 11,720 of 13,500 |
| Median mean coherence of valid pixels | 0.21 | 0.20 |
| Local velocity noise $\sigma_v$, 2017–2024/2022–2023 | 2.6/2.5 mm/yr | 2.6/2.6 mm/yr |

Furthermore, to elucidate the hydrological factors precipitating deformation, the reservoir water surface area is delineated using Sentinel-1 amplitude data. The characteristic low backscatter response of water bodies in SAR imagery is utilized due to specular reflection. Smooth water surfaces act like a mirror, reflecting the radar signal away from the sensor, resulting in very low backscatter values and appearing dark in SAR images [36,37]. Water pixels were separated from land by applying a fixed threshold of −16 dB to the VV backscatter of the Sentinel-1 GRD images [38], which are provided in Google Earth Engine as calibrated, terrain-corrected backscatter in decibels (collection COPERNICUS/S1_GRD; IW mode; 10 m pixel spacing); pixels with VV backscatter below −16 dB were classified as water. The same threshold was applied to all acquisitions, without scene-specific adjustment or speckle filtering, and images from all relative orbits covering the reservoir (ascending and descending) were used. The water surface area within the reservoir polygon was computed for each of the 88 acquisitions available between 2 June 2022 and 28 May 2023. The resulting surface-area series is used as a proxy for relative reservoir level changes; interferometric phase was not used over the water surface, because water surfaces decorrelate and do not provide reliable phase information. To test H2, the surface area was averaged within ±6 days of each InSAR epoch, and the mean displacement of the instrumented sector (LOS, east–west and vertical components, each linearly detrended over June 2022–May 2023) was correlated with it using the Pearson and Spearman coefficients at time lags of 0–48 days (displacement lagging the surface area). Because several components and lags were tested, a Bonferroni-corrected significance level of 0.005 (10 tests for the two decomposed components) was adopted.

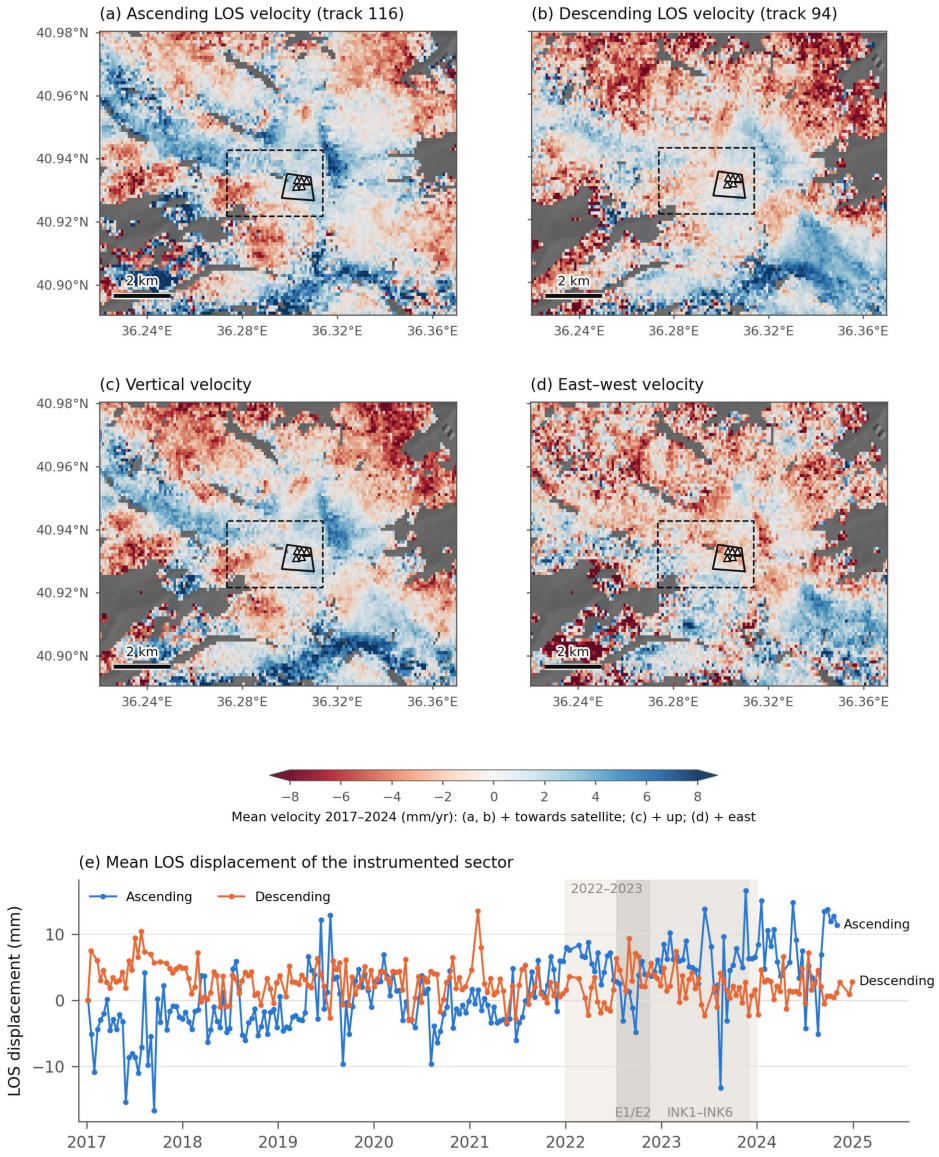



**Figure 3.** Mean velocities for 2017–2024 derived from Sentinel-1 interferograms: (**a**) ascending LOS velocity (track 116); (**b**) descending LOS velocity (track 94); (**c**) vertical and (**d**) east–west velocity components; (**e**) mean LOS displacement time series of the instrumented sector. Positive LOS values indicate motion towards the satellite. The solid polygon marks the instrumented sector, the dashed rectangle the extent of the susceptibility map (Section 3.3) and the triangles inclinometers INK1–INK6; grey areas are masked. Shading in (**e**) marks the 2022–2023 analysis period and the monitoring periods of inclinometers E1/E2 (17 July–17 November 2022) and INK1–INK6 (November 2022–November 2023).

### *2.4. Geophysical and Geotechnical Monitoring*

The geophysical and geotechnical data were collected during the site investigation of the landslide in November 2022 (Section 2.1). The five MASW lines (SİST-1 to SİST-5) were recorded with a 24-channel RAS-24 seismograph (Seistronix, Rancho Cordova, CA, USA). On each line, 12 geophones were placed at 5 m spacing (55 m spread), and shots were fired 10 m beyond both ends of the spread and at its centre. Rayleigh-wave dispersion curves were picked from common-midpoint gathers along each line in the frequency range of approximately 5–65 Hz and inverted for one-dimensional $V_s$ models to a depth of 30 m, which were interpolated to the two-dimensional sections shown in Section 3.4; the processing outputs reproduced in the report correspond to the SeisImager/SW package (Geometrics,

San Jose, CA, USA). The sampling interval, record length, source type, geophone model and software versions are not documented in the site investigation report. The five ERT profiles (ERT-1 to ERT-5), approximately 100 m (ERT-3) to 240 m long, were measured with a Mangusta TMG 255E multi-electrode resistivity system (Ambrogeo, Rivergaro, Italy) and inverted with RES2DINV (Geotomo Software, Penang, Malaysia), with a unit electrode spacing of 10 m, model depths of 25–43 m and absolute misfits of 2.4–5.8% after two iterations; the electrode array is not specified in the report. The positions of the lines and profiles are documented only on a location sketch in the site investigation report, without coordinates. They were transferred to Figure 2 by registering the background image of the sketch to the base map; the transferred MASW lines are 64–67 m long, consistent with the field geometry, but the positions are approximate, because the borehole positions marked in the sketch differ from the surveyed inclinometer coordinates by 7–36 m.

The MASW measurements are processed to obtain shear-wave velocity ($V_s$) profiles, which provide quantitative information on stiffness and stratigraphic layering within the slope materials. The fundamental principle of MASW involves generating surface waves and recording their propagation at multiple receivers. The phase velocity ($C$) of these waves is frequency dependent, a phenomenon known as dispersion. For a given frequency $f$, the phase velocity $C(f)$ is related to the wavelength $\lambda(f)$ by:

$$C(f) = f \cdot \lambda(f) \tag{4}$$

The shear-wave velocity profile ($V_s$) of the subsurface is then obtained by inverting the experimentally determined dispersion curve. The inversion process aims to minimize the discrepancy between the observed phase velocities ($C_{obs,i}$) and those predicted by theoretical models ($C_{theo,i}(V_s)$) for a given shear-wave velocity profile [39]. This is achieved by minimizing an objective function, often represented as the sum of squared differences [39]:

$$E = \sum_{i=1}^{n} \left(C_{obs,i} - C_{theo,i}(V_s)\right)^2 \tag{5}$$

where $n$ is the number of frequency points, $C_{obs,i}$ represents the observed phase velocity at frequency $i$, and $C_{theo,i}(V_s)$ denotes the theoretical phase velocity for a given shear-wave velocity profile ($V_s$). The theoretical phase velocities are calculated based on numerical methods for layered elastic media, where each layer is defined by its thickness, shear-wave velocity, P-wave velocity, and density. Because surface-wave inversion is non-unique and its resolution decreases with depth, the $V_s$ sections are interpreted in terms of layer averages rather than of individual contour values.

Inclinometer measurements provide cumulative displacement profiles with depth. The two inclinometers installed in 2020 (hereafter E1 and E2) were 30 m deep and equipped with 70 mm casings and were read with an RST Instruments (Maple Ridge, BC, Canada) digital inclinometer system; in the 2020 monitoring report, the positive A axis (A+) was oriented towards the reservoir, i.e., in the downslope direction. The six inclinometers installed in November 2022 (INK1–INK6) are 29.5–30.5 m deep. All casings were read at 0.5 m depth intervals in two orthogonal directions (A and B axes), and the profile changes were computed relative to the base reading assuming a fixed casing bottom, with bias correction applied by the data-reduction software. Displacement rates (Section 3.4) were computed for each 0.5 m reading depth and each interval between successive readings as the magnitude of the change in the A- and B-axis displacements divided by the length of the interval, and are given in mm/month; no interpolation in depth or time was applied. The orientation of the A axis of INK1–INK6 and the probe used in 2022–2023 are not documented in the available monitoring records; the displacements of these casings are therefore reported along the A and B axes, without conversion to a downslope direction.

An inclinometer measures the tilt of a casing installed in a borehole at regular depth intervals. The incremental lateral deviation ($\Delta L_i$) for a depth interval $i$ of length $l_i$ is calculated from the inclination angle ($\alpha_i$) with respect to the vertical:

$$\Delta L_i = l_i sin(\alpha_i) \quad (6)$$

The probe output $R_i$ (instrument reading units) is converted to the sine of the inclination angle through the instrument constant $K$ (reading units$^{-1}$), so that $sin\alpha_i = KR_i$ and the incremental displacement, in the same length unit as $l_i$, is:

$$\Delta D_i = R_i \cdot K \cdot l_i \quad (7)$$

The cumulative lateral displacement ($D_j$) at a given depth $j$ is then obtained by summing the incremental displacements from a fixed reference point (usually the bottom of the casing or a stable point) up to that depth:

$$D_j = \sum_{k=1}^{j} \Delta D_k \quad (8)$$

This cumulative displacement profile allows the horizontal displacement magnitude and direction to be determined along the depth of the casing. By analyzing these profiles over time, the rate of movement and the depth range of deformation can be assessed.

### *2.5. GIS-Based Landslide Susceptibility Mapping*

A GIS-based landslide susceptibility model was developed to spatially assess the environmental and geological conditions influencing slope instability, utilizing the Weighted Overlay method [25,40,41]. This approach enables the integration of multiple conditioning factors within a spatial decision framework. The selection of conditioning factors and their classification schemes was informed by established literature on landslide susceptibility [22,25,42], as well as the geological and hydrological characteristics of the Yaprak Dam region.

As delineated in Table 3, seven conditioning factors were incorporated into the analysis and categorized into four thematic groups: hydrological, topographical, geological, and environmental. The hydrological component comprised the Topographic Wetness Index, derived from the digital elevation model and the HydroSHEDS flow accumulation (Section 2.2), which delineates spatial variations in soil moisture potential and surface runoff accumulation [22]. Elevated TWI values were reclassified with correspondingly higher susceptibility ratings, indicative of increased potential for saturation-induced instability [22].

Topographical factors encompassed slope, aspect, and elevation, all derived from the SRTM DEM. Slope, expressed in percent, was classified into five categories. Aspect was classified according to slope orientation, thereby accounting for variations in solar insolation and moisture retention [22]. Elevation was incorporated to capture geomorphological differences that influence weathering rates and hydrological regimes across the reservoir [43]. Geological conditioning was represented by proximity to faults, extracted from the active fault database of the General Directorate of Mineral Research and Exploration [25]. Zones closer to fault structures were assigned higher susceptibility ratings, emphasizing the destabilizing influence of structural discontinuities and compromised rock integrity on slope stability [25]. Environmental factors were quantified through land use and vegetation density, using ESA WorldCover classifications and the NDVI from Sentinel-2 imagery [22]. Land use categories indicative of anthropogenic disturbance or sparse vegetative cover were assigned higher susceptibility ratings, while lower NDVI values indicated reduced root reinforcement and elevated susceptibility to surficial erosion [22]. Each conditioning

factor was reclassified into five susceptibility classes as detailed in Table 3. The relative weights (Section 3.3, Table 4) were assigned by the authors on the basis of previous studies [22,25] and expert judgement of the site conditions; no pairwise-comparison (AHP) procedure was applied, and the weights were entered directly in the weighted overlay. Because expert-assigned weights are subjective, the resulting map is interpreted as a relative susceptibility map, and the influence of the weights is evaluated with a sensitivity analysis (Section 3.3). The resulting weighted thematic layers were combined using the Weighted Overlay method to produce a landslide susceptibility map depicting the spatial distribution of relative susceptibility across the study area [25].

**Table 3.** GIS-based criteria definition and weighting methodology.

| Category | Factors/Criteria | Data Source | Unit | Suitability Score/Ranking (1–5) | Ref. |
|---|---|---|---|---|---|
| Hydrological | TWI | Derived from DEM | Index | (1) Very low (2) Low (3) Moderate (4) High (5) Very high | [22] |
| Topographical | Aspect | DEM | – | (1) Flat (2) N, NE (3) E, W (4) SE, SW (5) South | [43] |
| | Slope | DEM | Percent (%) | (1) 0–5 (2) 5–10 (3) 10–20 (4) 20–30 (5) >30 | |
| | Elevation | DEM | Meter (m) | (1) <500 (2) 500–600 (3) 600–700 (4) 700–800 (5) >800 | |
| Geological | Dist. to faults | MTA | Meter (m) | (1) >2000 (2) 1500–2000 (3) 1000–1500 (4) 500–1000 (5) 0–500 | [25] |
| Environmental | Land use | ESA WorldCover | Class | (1) Forest, grassland [a], permanent water [a] (2) Shrub (3) Cropland (4) Built-up (5) Bare | [22] |
| | NDVI | Sentinel-2 | Index | (1) >0.6 (2) 0.4–0.6 (3) 0.2–0.4 (4) 0.1–0.2 (5) <0.1 | |

Note: [a] Grassland (ESA WorldCover class 30) and permanent water (class 80) were not reclassified before the overlay and were assigned a score of 1 in the weighted overlay; the effect of scoring them as 2 and 5 is evaluated in Section 3.3.

**Table 4.** General and final weights of main and sub-criteria used in the landslide susceptibility model.

| General Weight | Main Criteria | Sub-Criteria | Final Weight | Rank |
|---|---|---|---|---|
| 0.45 | Topographical conditions | Slope | 0.30 | 1 |
| | | Elevation | 0.10 | 4 |
| | | Aspect | 0.05 | 6 |
| 0.20 | Hydrological conditions | Topographic Wetness Index (TWI) | 0.20 | 2 |
| 0.20 | Geological conditions | Distance to faults | 0.20 | 3 |
| 0.15 | Environmental conditions | Land use/cover | 0.10 | 5 |
| | | NDVI | 0.05 | 7 |
| 1.00 | Total | | 1.00 | – |

To test H3, the susceptibility map was compared with the InSAR velocities at the InSAR pixel scale. Each 0.001° InSAR pixel was assigned the majority class of the map cells that it contains (pixels containing fewer than four map cells were excluded), and pixels whose ascending or descending velocity exceeded $2\sigma_v$ in absolute value were labelled as InSAR anomalies. For each class, the frequency ratio FR = (percentage of anomaly pixels in the class)/(percentage of pixels in the class) was calculated; FR > 1 indicates that anomalies occur more often than expected from the areal extent of the class. The association between

class and anomaly occurrence was tested with a chi-square test. Because the model was not calibrated with InSAR data and no independent landslide inventory is available, this comparison is a consistency check, not a validation of the predictive power of the model.

To assess the influence of the expert-assigned weights, the weighted overlay was first reproduced from the reclassified factor layers of the original GIS project; the reproduction yielded identical classes in all 8124 cells of the map, with the weighted sum rounded to the nearest integer. Each weight was then changed by ±20%, while the other weights were rescaled proportionally to keep the total at 100%. In addition, equal weights, an overlay without the distance-to-faults factor, the land-use scores of grassland and water discussed under Table 3, and 1000 random weight sets drawn from a Dirichlet distribution centred on the original weights (concentration parameter 57, i.e., a coefficient of variation of 20% for the largest weight) were evaluated. For each scenario, the percentage of cells that change class, the Spearman correlation between the continuous weighted scores and those of the original map, and the frequency-ratio test described above were computed (for 200 of the Monte Carlo runs in the case of the frequency-ratio test).

## 3. Results

In this study, slope instabilities at the Yaprak Dam site were investigated through four complementary perspectives: remote sensing-based deformation analysis (InSAR), hydrological assessment, geophysical and geotechnical field measurements, and GIS-based susceptibility modeling. The results obtained from each analytical component are presented in the following subsections.

### *3.1. Surface Deformation from Multi-Temporal InSAR*

Figure 3 shows the mean velocities for 2017–2024 in the ascending and descending geometries and the vertical and east–west components derived from them. Outside the landslide area, the velocities vary spatially by a few millimetres per year (standard deviation of 3.7 mm/yr in the ascending and 4.0 mm/yr in the descending geometry), with patterns that partly follow valleys and ridges and are therefore attributed mainly to residual tropospheric and processing noise rather than to ground motion. Within the extent of the susceptibility map, 90% of the valid pixels have velocities between −4.0 and +3.4 mm/yr (ascending) and between −2.7 and +1.9 mm/yr (descending).

In the instrumented sector (87 ascending and 88 descending valid pixels; mean slope of about 16° and mean aspect of about 218°, i.e., south-west-facing, at the 100 m resolution of the InSAR products), the mean LOS velocity was +1.6 mm/yr (ascending; pixel range −0.4 to +3.7 mm/yr) and −0.3 mm/yr (descending; −3.3 to +3.2 mm/yr) for 2017–2024, and +1.2 mm/yr (ascending) and −1.1 mm/yr (descending) for 2022–2023. The corresponding east–west component was −1.7 mm/yr (2017–2024) and −2.1 mm/yr (2022–2023; pixel range −6.0 to +0.3 mm/yr), i.e., westward, and the vertical component was +0.9 and +0.1 mm/yr, respectively. A westward motion is compatible with downslope movement of the south-west-facing slope; if the entire east–west component reflected horizontal movement in the direction of the aspect, the corresponding horizontal rate would be about 3 mm/yr (2.1 mm/yr divided by $|\sin 218°| \approx 0.62$). However, all sector-mean velocities are smaller than $2\sigma_v$ (approximately 5 mm/yr, Table 2) and are therefore not significant; H1 is not supported at the resolution of the data. The difference between the 2017–2024 and 2022–2023 velocities is less than 1 mm/yr in each geometry and component. The mean time series of the sector (Figure 3e) show epoch-to-epoch fluctuations of several millimetres, annual amplitudes of 1.6 mm (ascending) and 0.7 mm (descending), and no acceleration during July–November 2022 or during the monitoring period of INK1–INK6.

### *3.2. Reservoir Surface Area and Deformation*

To investigate the potential hydrological controls on the observed surface deformation, temporal variations in reservoir water surface area were analyzed together with radar backscatter signals derived from satellite data (Figure 4). The surface-area series shows large differences between consecutive acquisitions (approximately 0.5–2.3 km$^2$), and a regular seasonal cycle is not clearly resolved over the single year of observations.

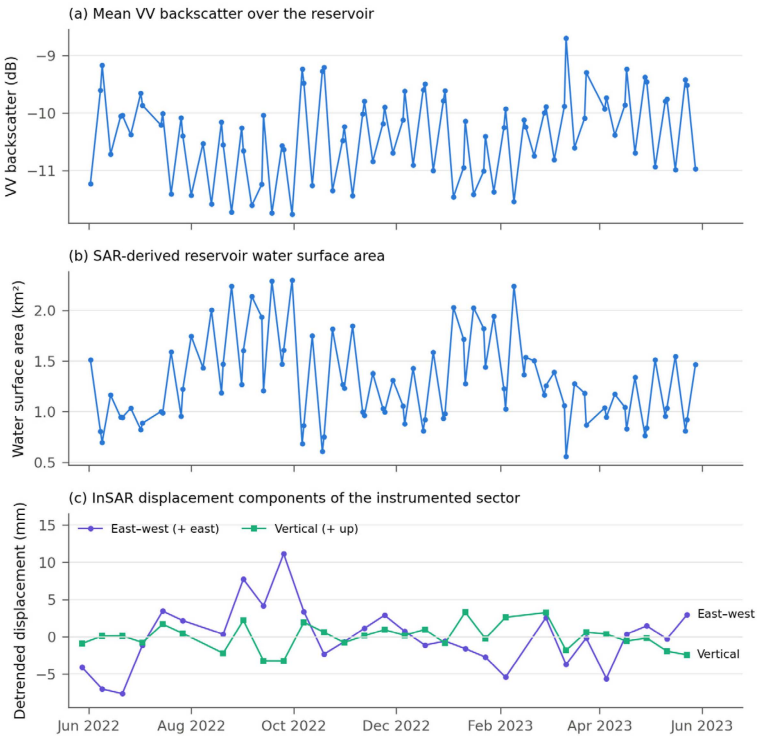



**Figure 4.** Reservoir surface-area proxy and InSAR displacement, June 2022–May 2023: (**a**) mean VV backscatter over the reservoir; (**b**) SAR-derived reservoir water surface area (km$^2$); (**c**) linearly detrended east–west and vertical displacement of the instrumented sector.

Figure 4c compares the surface-area series with the detrended east–west and vertical displacements of the instrumented sector. The east–west displacement showed the strongest association with the surface area at zero lag (Pearson $r = 0.39$, $p = 0.035$; Spearman $\rho = 0.34$, $p = 0.071$; $n = 29$), which decreased at a lag of 12 days ($r = 0.32$, $p = 0.094$) and vanished at longer lags; the vertical displacement showed no association ($|r| \leq 0.12$, $p \geq 0.56$). The LOS series gave similar results (ascending: $r = -0.41$, $p = 0.023$ at zero lag; descending: $r \leq 0.33$, $p \geq 0.08$). None of these correlations is significant at the Bonferroni-corrected level of 0.005. The sign of the east–west correlation, i.e., a smaller surface area associated with a more westward (downslope) position, would be consistent with a drawdown effect, but given the noise of the single-epoch displacements, the length of the series and the number of tests, H2 cannot be confirmed. Reservoir level and pore pressure records were not available, and rainfall, snowmelt and temperature were not analyzed; the hydrological interpretation therefore remains a hypothesis (Section 4.3).

### *3.3. GIS-Based Susceptibility Modeling*

To delineate areas of elevated susceptibility at the Yaprak Dam site, a GIS-based multi-criteria evaluation framework was implemented. Within this framework, seven conditioning factors representing the dominant geoenvironmental characteristics of the study area were generated and analyzed (Figure 5). These factors include slope, aspect, elevation, TWI,

distance to faults, land use, and NDVI. The selected factors are widely used in landslide susceptibility studies and were chosen based on literature review and site-specific geomorphological and hydrological conditions.

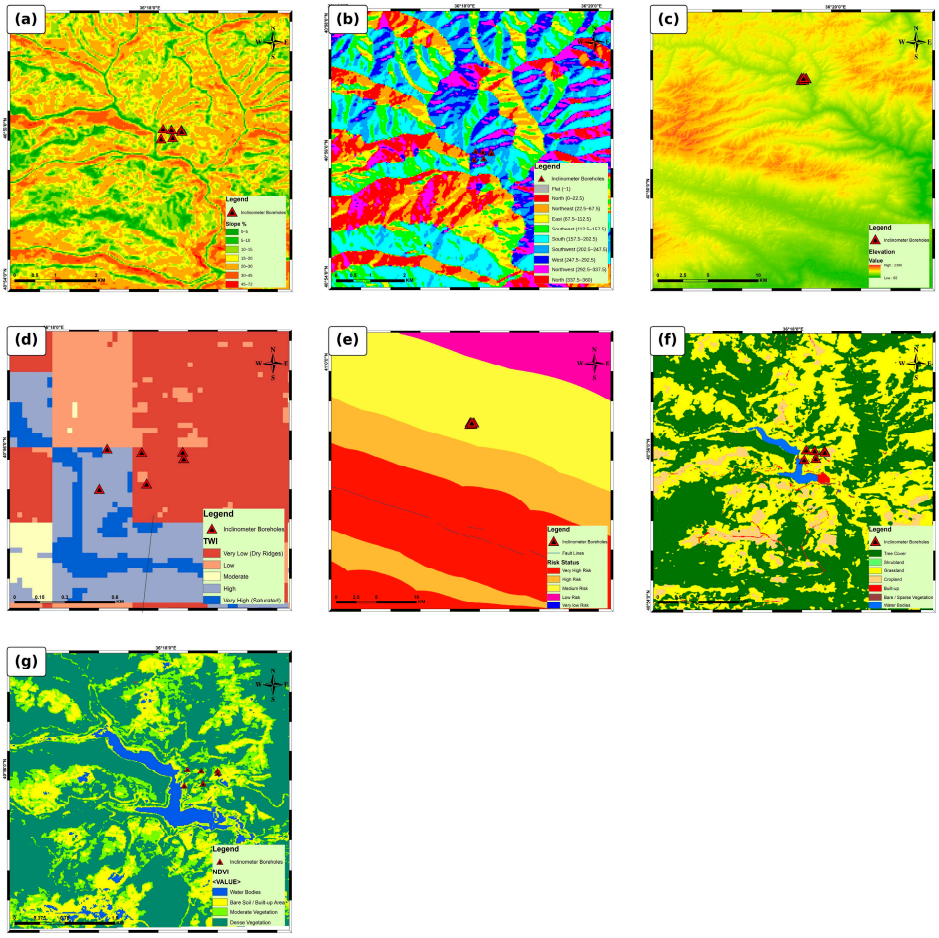



**Figure 5.** Conditioning factors used in the landslide susceptibility analysis: (**a**) slope; (**b**) aspect; (**c**) elevation; (**d**) Topographic Wetness Index (TWI); (**e**) distance to faults; (**f**) land use; (**g**) Normalized Difference Vegetation Index (NDVI).

The original thematic layers were first standardized through a reclassification process to ensure comparability across different data types and units. Each factor was reclassified into a common susceptibility scale ranging from 1 (very low susceptibility) to 5 (very high susceptibility), according to its relative influence on slope instability. The spatial distributions of the original conditioning factors are presented in Figure 5, while the corresponding reclassified layers are shown in Figure 6.

Slopes along the reservoir margins commonly range between 10% and 30% (Figure 5a), and the instrumented sector lies on a south-west-facing slope (Figure 5b). High TWI values are concentrated along reservoir shorelines and valley bottoms (Figure 5d). Areas within 500 m of mapped fault traces fall into the highest distance-to-fault class (Figure 5e). The land use and NDVI layers (Figure 5f,g) show sparsely vegetated or bare surfaces mainly along the reservoir margins affected by water level fluctuations.

The general and final weights used in the susceptibility model are summarized in Table 4 (the weighting procedure is described in Section 2.5).

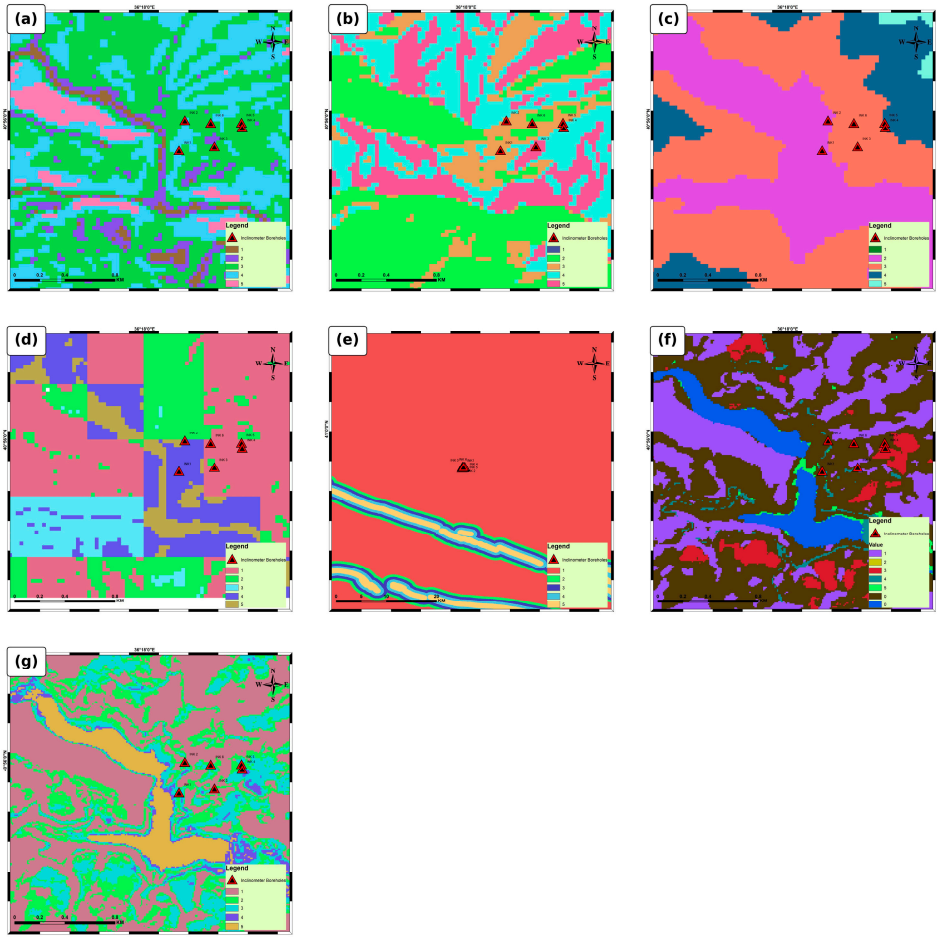



**Figure 6.** Spatial distribution of reclassified conditioning factors used in the susceptibility analysis. All factors were reclassified into a common susceptibility scale ranging from 1 (very low) to 5 (very high). (**a**) Slope; (**b**) aspect; (**c**) elevation; (**d**) Topographic Wetness Index (TWI); (**e**) distance to faults; (**f**) land use; (**g**) NDVI. The colours are specific to each sub-figure and are explained in its legend; in (**f**), the value 0 denotes grassland and permanent water, which were not reclassified and were assigned a score of 1 in the weighted overlay (Table 3).

The reclassified and weighted layers were then integrated using the Weighted Overlay method to produce the final susceptibility map (Figure 7). To test H3, the map was compared with the InSAR velocities and with the locations of the inclinometer boreholes.

The final map is dominated by the Low (69.9% of the cells) and Moderate (29.8%) classes; the Very Low and High classes cover 0.1% and 0.2% (19 cells) of the map, and no cell was assigned to the Very High class. Inclinometers INK1 and INK2 lie in the Moderate class and INK3–INK6 in the Low class. At the InSAR pixel scale, the 789 pixels covered by the map are assigned to the Low (554 pixels) and Moderate (235 pixels) classes; the Very Low and High classes are too small to form the majority of any 100 m pixel. Only 18 pixels (2.3%) showed a significant velocity ($|v| > 2\sigma_v$ in at least one geometry) in 2017–2024, and 17 pixels in 2022–2023. These anomalies were distributed between the Low and Moderate classes approximately in proportion to their area (Table 5): the frequency ratio of the Moderate class was 1.12 (2017–2024) and 1.18 (2022–2023), and the chi-square test showed no association between class and anomaly occurrence ($p = 0.94$ and $p = 0.81$). H3 is therefore not supported: at the resolution of the available InSAR data, the susceptibility map does not discriminate between deforming and non-deforming ground (Section 4.4).

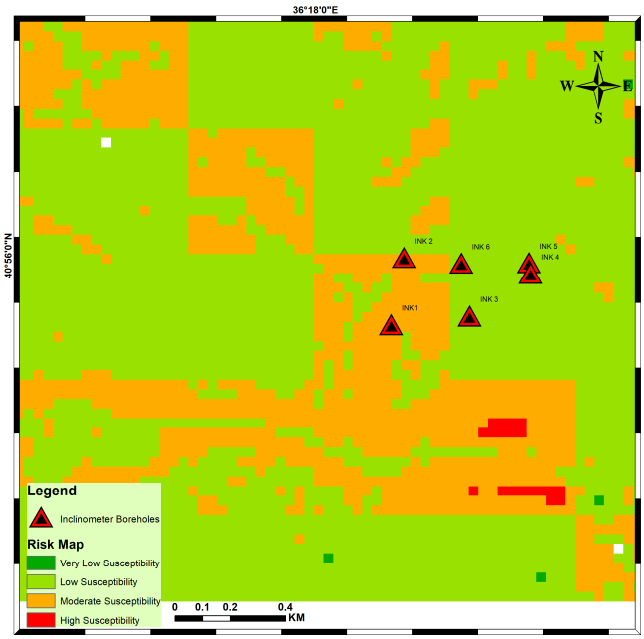



**Figure 7.** Final landslide susceptibility map produced using the weighted overlay method, showing the spatial distribution of susceptibility classes and the locations of inclinometer boreholes.

**Table 5.** Distribution of InSAR anomaly pixels ($|v| > 2\sigma_v$) among the susceptibility classes and frequency ratios (FR).

| Susceptibility Class | InSAR Pixels (% of Area) | Anomalies 2017–2024 (% of Anomalies) | FR 2017–2024 | Anomalies 2022–2023 (% of Anomalies) | FR 2022–2023 |
|---|---|---|---|---|---|
| Low | 554 (70.2) | 12 (66.7) | 0.95 | 11 (64.7) | 0.92 |
| Moderate | 235 (29.8) | 6 (33.3) | 1.12 | 6 (35.3) | 1.18 |
| Total | 789 (100) | 18 (100) | – | 17 (100) | – |

Reproducing the overlay showed that two factors provide little spatial contrast within the mapped area: all cells lie more than 2000 m from the mapped faults and therefore have the same distance-to-faults score (1), and 92% of the cells have a land-use score of 1, including grassland (48% of the cells) and the water surface of the reservoir (4%). The constant fault score shifts all weighted scores equally; it does not change their ranking, but it affects the assignment of cells to the integer classes. The sensitivity analysis (Table 6) shows that the ranking of the cells is robust (Spearman ρ between the weighted scores and those of the original map ≥ 0.98 for ±20% changes of individual weights, 0.69 for equal weights and ≥0.87 in 95% of the Monte Carlo runs), whereas the class boundaries are less stable: ±20% changes of individual weights reassign 0.2–9.0% of the cells, equal weights 19.1%, and the Monte Carlo weight sets 4.5–27.2% (5th–95th percentile), with the Moderate and High classes covering 11.9–53.5% of the map. Scoring grassland and water as 2 and 5 would reassign 6.2% of the cells. The inclinometers remain in the same classes in all deterministic scenarios except the overlay without the distance-to-faults factor, in which INK2 moves to the High class. In none of the scenarios did the InSAR anomalies show a significant association with the Moderate and High classes (frequency ratios 0.86–1.55, chi-square $p \geq 0.22$; Monte Carlo: $p \geq 0.10$), so the conclusion that the map is not supported by the InSAR data does not depend on the choice of weights.

**Table 6.** Sensitivity of the susceptibility map and of the InSAR consistency check to the factor weights. FR: frequency ratio of InSAR anomaly pixels in the Moderate and High classes; values for −20%/+20% changes of the weight of the named factor.

| Scenario | Cells Changing Class (%) | Moderate + High Area (%) | FR 2017–2024 | FR 2022–2023 |
|---|---|---|---|---|
| Original weights (Table 4) | – | 30.0 | 1.12 | 1.18 |
| Slope −20%/+20% | 7.0/8.9 | 23.3/37.9 | 1.45/1.04 | 1.28/1.11 |
| TWI −20%/+20% | 7.8/4.2 | 29.3/29.8 | 1.40/1.12 | 1.27/1.18 |
| Distance to faults −20%/+20% | 7.3/9.0 | 37.2/21.3 | 1.23/1.08 | 1.47/0.86 |
| Elevation −20%/+20% | 2.7/1.4 | 27.4/29.1 | 1.22/1.17 | 1.07/1.24 |
| Land use −20%/+20% | 0.2/3.3 | 29.8/26.8 | 1.13/1.25 | 1.20/1.11 |
| Aspect −20%/+20% | 3.3/0.2 | 26.9/29.8 | 1.25/1.13 | 1.11/1.20 |
| NDVI −20%/+20% | 1.1/2.4 | 29.0/27.7 | 1.14/1.25 | 1.21/1.10 |
| Equal weights | 19.1 | 25.5 | 1.46 | 1.55 |
| Without distance to faults | 37.1 | 64.5 | 1.12 | 1.09 |
| Grassland = 2, water = 5 | 6.2 | 36.1 | 1.11 | 1.35 |
| Monte Carlo (5th–95th percentile) | 4.5–27.2 | 11.9–53.5 | 0.31–1.44 | 0.39–1.47 |

### *3.4. Subsurface Characterization: Geophysical and Geotechnical Evidence*

The MASW sections (Figure 8) show shear-wave velocities that increase with depth along all five lines. The layer models of the site investigation report (Table 7) define an upper layer about 7–16 m thick with average $V_s$ of 320–596 m/s, underlain by layers with average $V_s$ of 495–833 m/s; the time-averaged velocity of the upper 30 m ($V_{s30}$) ranges from 432 to 745 m/s. The lowest values (281–309 m/s) occur in the uppermost few metres of line SİST-3. The lower-velocity upper layer is consistent with the weathered phyllite, debris and sandy–silty–clayey soils described in the boreholes, while the higher velocities at depth correspond to moderately hard to massive phyllite. Shear-wave velocity alone cannot establish the degree of saturation or the shear strength of these materials; the ERT results of the same investigation, which identify a low-resistivity clay zone in the area of boreholes SK-4 and SK-5 and fractured phyllite in the upper part of the profiles, provide supporting but indirect evidence of weaker, more conductive near-surface materials. Groundwater levels in the boreholes are not reported in the available site investigation documents; seepage springs around the landslide indicate groundwater flow within the slope (Section 4.3), and the report recommends determining the groundwater flow direction and installing drainage lines, but the groundwater conditions could not be quantified in this study.

The inclinometer records are summarized in Figures 9 and 10. In the six inclinometers installed in November 2022 (INK1–INK6), readings were taken on 28/29 November 2022 (base), 16 December 2022, 5 January, 3 February and 7 March 2023, and on 4 April 2023 (INK1) or 29 November 2023 (INK2–INK6), as recorded in the instrument data sheets. The monitoring periods therefore differ: INK1 covers 126 days, INK2–INK6 cover 365–366 days, and INK2–INK6 were not read between 7 March and 29 November 2023. The cumulative displacements at the last reading are small: along the A axis they reach 2.8 mm (INK1), 2.8 mm (INK2), 3.5 mm (INK3), 4.6 mm (INK4), 7.8 mm (INK5) and 7.9 mm (INK6), with the largest values at the top of the casings, and they do not exceed 2.7 mm along the B axis. In INK5 and INK6, the A-axis displacements fall below 1 mm at depths of about 7.5–9.5 m. Because of the different periods, the casings are compared over the period common to all six: by 7 March 2023 (98–99 days), the A-axis displacement at the top of the casings was 1.6–7.0 mm, and most of the displacement of INK2–INK6 had occurred by then; between 7 March and 29 November 2023 (267 days), it increased by only 0.8–1.6 mm (1.1–2.2 mm/yr). Annualizing the 126-day record of INK1 (about 8 mm/yr) would therefore probably overestimate its long-term rate. The rates in Figure 9 are highest in the short first interval of 17–18 days (up to about 10 mm/month), in which reading errors have the largest effect on the rate, and the increments between successive readings include reversals of up

to about 1.5 mm at the top of INK1 and INK3. Displacements of a few millimetres are close to the range in which systematic errors of probe inclinometer surveys become significant; these records are therefore interpreted as indicating low rates of near-surface movement during the monitoring period, not as resolving a discrete shear surface.

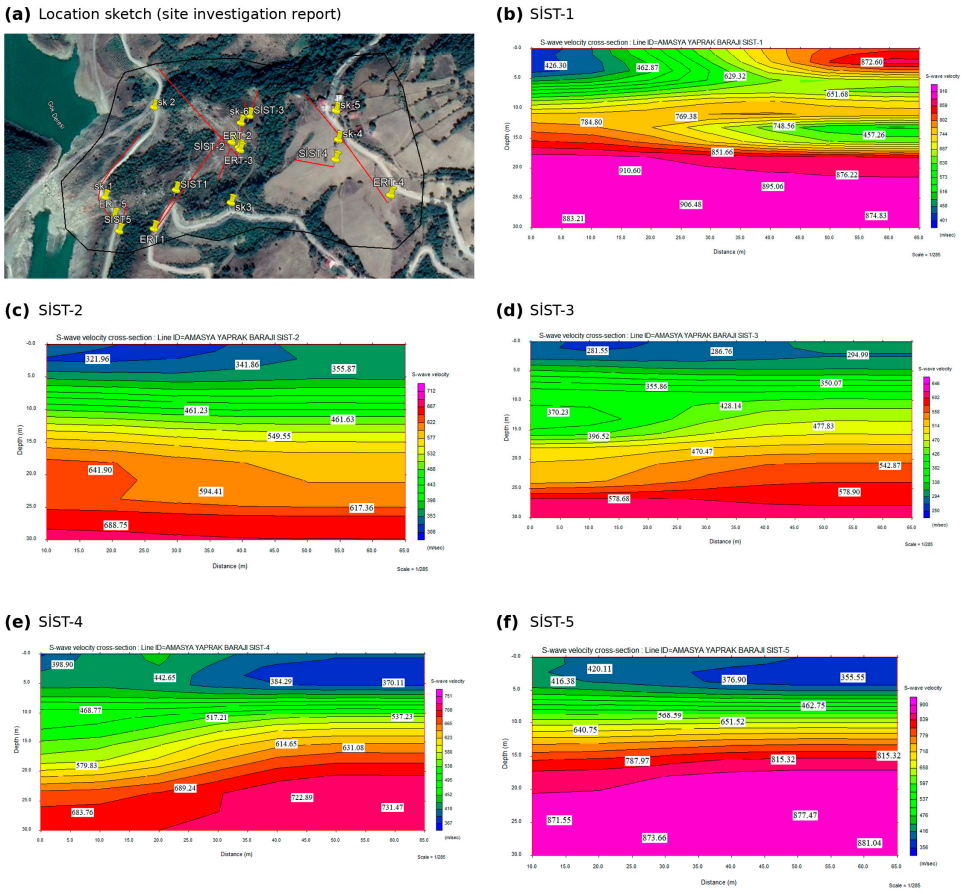



**Figure 8.** Two-dimensional shear-wave velocity ($V_s$) sections along the MASW lines of the site investigation: (**a**) location sketch of the MASW lines (SİST), ERT profiles and boreholes (sk) from the site investigation report (positions approximate; see Figure 2); (**b**–**f**) sections of lines SİST-1 to SİST-5. Each section has its own colour scale (m/s).

**Table 7.** Layer-average shear-wave velocities of the MASW lines (from the site investigation report).

| Line | Upper Layer Depth (m) | Upper Layer $V_s$ (m/s) | Lower Layer(s) $V_s$ (m/s) | $V_{s30}$ (m/s) |
|---|---|---|---|---|
| SİST-1 | 0–8.9 | 596 | 833 | 745 |
| SİST-2 | 0–7.0 | 338 | 495 (7.0–15.6 m); 632 (15.6–30 m) | 494 |
| SİST-3 | 0–8.9 | 320 | 506 | 432 |
| SİST-4 | 0–15.6 | 463 | 669 | 547 |
| SİST-5 | 0–8.9 | 459 | 807 | 660 |

Larger displacements were recorded earlier in the two inclinometers installed in 2020 (E1 and E2). Between 17 July and 17 November 2022, the cumulative A-axis displacement at the top of the casings reached 24.9 mm (E1) and 20.6 mm (E2), directed towards the reservoir, while B-axis displacements remained below 3.5 mm. In both casings the displacement decreases gradually with depth, without a sharp offset that would indicate a discrete shear surface; it falls below 1 mm at about 20 m in E1 and at about 27 m in E2; the 2022 site investigation report attributes these readings to the inclinometer casings that existed on the slope before the investigation.

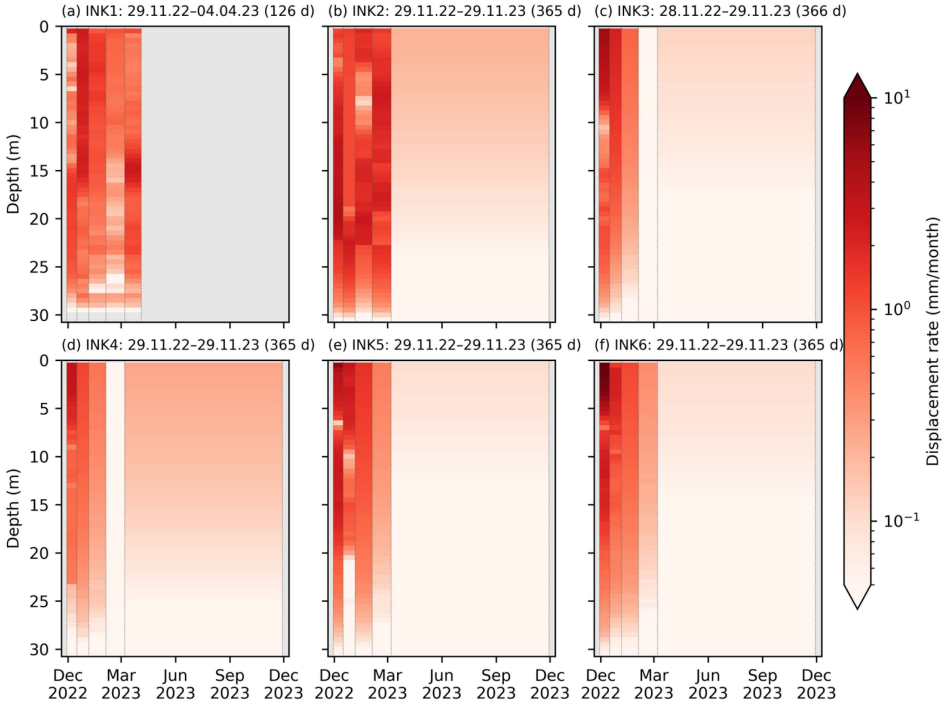



**Figure 9.** Displacement rates in inclinometer boreholes INK1–INK6, computed for each 0.5 m reading depth and each interval between successive readings as the magnitude of the change in the A- and B-axis displacements divided by the length of the interval (mm/month, logarithmic colour scale). Each cell spans one reading interval (dotted lines mark the reading dates); no interpolation was applied, and grey indicates periods without readings. Sub-figures (**a**–**f**) show INK1–INK6; the panel titles give the monitoring period of each casing (dd.mm.yy) and its length in days (d).

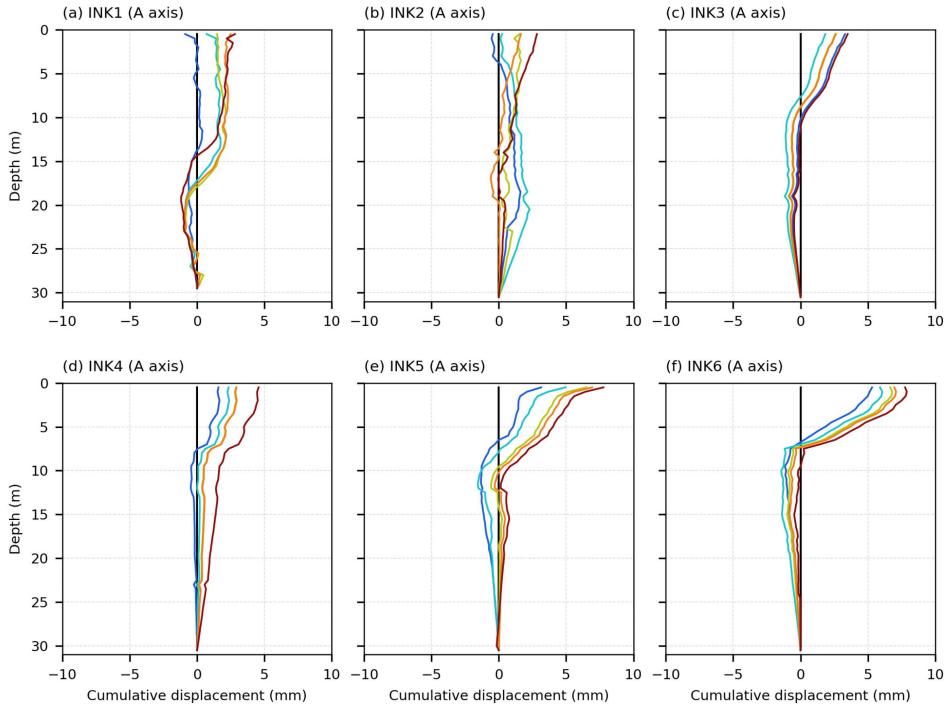



**Figure 10.** Cumulative lateral displacement profiles along the A axis measured in inclinometer boreholes INK1–INK6 (**a**–**f**). The solid black line is the base reading (zero displacement), relative to which the displacements of the subsequent readings are computed; the last reading is on 4 April 2023 for INK1 and on 29 November 2023 for INK2–INK6. The orientation of the A axis is not documented (Section 2.4).

Taken together, the subsurface data show (i) a lower-velocity, weathered near-surface zone whose thickness varies between about 7 and 16 m along the MASW lines, and (ii) downslope displacements that are largest at the surface and decrease with depth, reaching about 20–27 m in the 2020 inclinometers. The displacement profiles do not identify a single sliding surface within the 30 m casings, and the gradual decrease in displacement with depth is compatible with distributed deformation of the weathered slope mass. The available data do not allow the mechanism (e.g., creep versus intermittent sliding) to be determined, and deformation below the depth of the casings cannot be excluded (Section 4.5). At laboratory and constitutive-model scale, time-dependent (creep) deformation and loading-rate effects have been shown to govern the approach of granular materials to a critical state [44,45]; establishing whether such behavior controls the Yaprak slope would require longer monitoring records and laboratory testing of the slope materials.

## 4. Discussion

### *4.1. Contribution of the Integrated Workflow and Relevance for Sustainable Dam Management*

The study combines four information sources that are often analyzed separately: two-geometry Sentinel-1 InSAR time series, SAR-derived reservoir surface area, a GIS-based susceptibility model and site-investigation data (MASW, ERT, boreholes and inclinometers). Compared with dam-focused InSAR studies, which mainly address the deformation of the dam body or its agreement with geodetic surveys [9,12,16,22,23], the focus here is a reactivated landslide on a reservoir slope; compared with regional studies that combine InSAR and susceptibility mapping [17,19], the analysis is carried out at site scale with explicit, quantitative tests. The main result is largely negative: for 2017–2024 and for 2022–2023, freely available InSAR products did not detect motion of the instrumented sector above about 5 mm/yr, and they did not support the spatial pattern of the susceptibility map. For the sustainable management of dams, this is nevertheless useful information. Open access InSAR can exclude fast movements of reservoir slopes at very low cost and over long periods, but only for moving areas that are large compared with the resolution of the products (about 100 m) and for movement components to which the acquisition geometries are sensitive. On the south-west-facing Yaprak slope, a downslope movement is observed mainly through its east–west component, which is smaller than its north component, and north–south motion is practically not observed. The detection threshold, resolution and directional sensitivity must therefore be quantified before the results are used to prioritize monitoring, and slow or localized movements such as those recorded by the inclinometers still require in situ instruments.

Four lessons from this case can be transferred to other reservoir slopes. First, the local detection threshold of InSAR velocities (here about 5 mm/yr, $2\sigma$) should be estimated empirically before any velocity is interpreted, because the formal uncertainties of the time-series fit underestimate it by more than an order of magnitude. Second, the sensitivity of the available geometries to the expected direction of movement should be checked; on the south-west-facing Yaprak slope, the north component of a downslope movement, to which Sentinel-1 is nearly insensitive, is the larger of the two horizontal components. Third, InSAR results should be compared with in situ data of the same period, which in this study revealed both agreement (INK1–INK6) and a limitation (E1/E2). Fourth, susceptibility maps used for screening should be tested statistically against independent observations, together with the sensitivity of the result to the weights, and checked for factors that do not vary within the study area, such as the distance to faults here.

### *4.2. Comparison of InSAR and Inclinometer Observations*

The InSAR results are consistent with the six inclinometers installed in November 2022, which recorded 2.8–7.9 mm of displacement at the top of the casings over 126 days (INK1) to about one year (INK2–INK6), most of it between November 2022 and March 2023. Over one year, INK2–INK6 moved 2.8–7.8 mm at the top of the casings; even if directed downslope (towards 218°), rates of this size would project onto the ascending and descending lines of sight at no more than about 3 mm/yr, below the local detection threshold, and the westward component of about 2 mm/yr is compatible in direction and order of magnitude with downslope movement of the south-west-facing slope. In contrast, the 20.6–24.9 mm recorded by E1 and E2 between July and November 2022 would correspond to 60–75 mm/yr if sustained, which was not observed in the sector-mean time series. Possible reasons for this discrepancy are (i) the position of E1 and E2, which the location sketch of the 2020 monitoring report places within the landslide area but whose coordinates are not documented, so that their position relative to the instrumented sector cannot be checked; (ii) the multilooking of the LiCSAR products to approximately 100 m, which averages the displacement of a small or narrow moving mass with that of stable ground; (iii) the low sensitivity of both geometries to north–south motion, which on a slope facing 218° represents the larger part of the horizontal downslope component ($|\cos 218°| \approx 0.79$); and (iv) loss of coherence on moving or vegetated ground. Full-resolution processing (e.g., persistent and distributed scatterers), artificial corner reflectors or higher-resolution SAR data would be required to monitor the slope at the scale of the inclinometers. The eight-year record also addresses the question of whether the 2022–2023 behaviour is anomalous: the velocities of the sector in 2022–2023 differ from the 2017–2024 mean by less than 1 mm/yr, and the time series show no acceleration in the period covered by the inclinometers.

### *4.3. Hydrological Interpretation and Alternative Explanations*

The site investigation report interprets the movement as the reactivation of an old landslide after impoundment, caused by the saturation of its toe, and the presence of seepage springs indicates groundwater flow within the slope. Reservoir drawdown is a well-known destabilizing factor for such slopes, and its effect on stability has been quantified with limit-analysis and reliability approaches for different drawdown rates [13–15]. Drawdown also unloads the toe of the slope; laboratory studies on filled discontinuities show that the unloading rate and the geometry of the sliding interface control whether slip develops in a stable or unstable manner [46]. The correlation analysis (Section 3.2), however, did not provide significant evidence of a relation between reservoir surface area and displacement. This does not exclude a hydromechanical control: the surface-area proxy covers only one year, shows large differences between consecutive acquisitions and is an indirect measure of the water level, while the InSAR displacements of individual epochs have a noise of several millimetres. Testing the drawdown hypothesis requires reservoir level records, piezometers in the slope, rainfall and snowmelt data and longer overlapping time series, which would also allow formal methods such as transfer-function or Granger-causality analysis to be applied. Alternative or additional drivers include rainfall and snowmelt infiltration, which can raise groundwater levels independently of the reservoir; seasonal temperature and freeze–thaw effects on the near-surface materials; consolidation of fill materials, which would produce a predominantly vertical signal; and seismic shaking in this active tectonic setting.

### *4.4. Consistency of the Susceptibility Map*

The weighted overlay map was not calibrated or validated with an independent data set, and the comparison with InSAR (Table 5) did not reveal a higher occurrence of InSAR

anomalies in the higher susceptibility classes; the sensitivity analysis (Table 6) shows that this conclusion does not depend on the weights, although the class boundaries themselves do. This result does not prove that the model is wrong, because (i) significant InSAR anomalies are rare in the study area and some of them may be noise; (ii) the map is dominated by two classes within an area of about 3 km × 2 km, so its contrast is limited; and (iii) the InSAR pixels are about three times larger than the map cells, and the High class (19 cells) is smaller than a single InSAR pixel. Moreover, InSAR anomalies represent ground movement during the observation period rather than mapped failures; even a positive spatial agreement would therefore indicate consistency with current deformation rather than predictive power. A predictive validation would require a landslide inventory divided into independent training and test sets, or a temporal split of past events, and metrics such as the area under the receiver operating characteristic curve [41,42]. In addition, the 30 m SRTM DEM smooths the topography of the dam and of the reservoir margins, which affects the slope, aspect and TWI layers; site-scale susceptibility mapping would benefit from a high-resolution DEM, for example from UAV photogrammetry or LiDAR.

### *4.5. Limitations*

The following limitations should be considered when interpreting the results. (i) The LiCSAR products are multilooked to approximately 100 m, and the mean coherence on the slope is about 0.2, so small or narrow moving areas may not be resolved; both geometries are nearly insensitive to north–south motion. (ii) GACOS tropospheric corrections were not available for all epochs; the empirical correction of offset, ramp and elevation-dependent phase refers all velocities to the surrounding area and may partly remove long-wavelength deformation. (iii) The reservoir proxy covers one year, was derived with a fixed threshold from images acquired in different geometries, which may add scatter to the series (e.g., through differences in incidence angle and wind roughening of the water surface), and was not calibrated against gauge levels, and no piezometric or groundwater-level, rainfall or snow data were available. (iv) The displacements recorded in INK1–INK6 are of the order of a few millimetres, and the E1/E2 readings used here cover only four months. (v) The casings are 30 m deep and the MASW lines investigate the upper 30 m, so deformation at greater depths cannot be excluded; moreover, the assumption of a fixed casing bottom would underestimate displacements if movement extends to that depth. (vi) MASW provides smoothed, non-unique $V_s$ models, and $V_s$ alone cannot establish saturation or strength. (vii) No laboratory strength parameters, pore pressure data or stability analyses (limit equilibrium or numerical) were available, so factors of safety and the mechanical behavior of the slope could not be quantified; once such data are available, drawdown-specific limit-analysis and reliability methods [14,15] and data-driven stability assessment approaches, such as the explainable machine-learning framework developed for tunnels in rock masses [47], could be adapted to the reservoir slope. (viii) The susceptibility weights were assigned by expert judgement; the class boundaries depend on them (Table 6), and two factors (distance to faults and land use) provide little spatial contrast within the mapped area. (ix) The 30 m SRTM DEM limits the topographic detail of the susceptibility factors, and the TWI combines the 30 m slope with a much coarser flow accumulation (15 arc-seconds) [48], so that it represents only the broad pattern of drainage.

Beyond these limitations, the integration of the monitoring data could be improved with methods that exploit their temporal and spatial structure. Time-series clustering based on soft dynamic time warping (Soft-DTW) groups series with similar temporal behaviour even when they are shifted in time, and graph neural networks learn dependencies between irregularly distributed observation points; He et al. [49] combined both in a framework for the spatiotemporal prediction of groundwater contamination. For reservoir slopes, such

methods could be used to group InSAR pixels and inclinometers with similar displacement histories and to relate them to reservoir and groundwater levels, but they require longer and denser records than are available here, in particular regular inclinometer readings and reservoir level and piezometric data.

## 5. Conclusions

This study combined two-geometry Sentinel-1 InSAR time series, SAR-derived reservoir surface area, a GIS-based susceptibility model and site-investigation data to test three hypotheses on the deformation of the left-bank reservoir slope of the Yaprak I Dam. The main findings are as follows:

(1) InSAR time series for 2017–2024 (230 ascending and 224 descending epochs) show no significant motion of the instrumented sector: mean LOS velocities were between −1.1 and +1.6 mm/yr, and the east–west and vertical components were −2.1 and +0.1 mm/yr in 2022–2023, all below the local noise level of about 5 mm/yr ($2\sigma$). The small westward component is compatible with downslope movement of the south-west-facing slope, and the 2022–2023 velocities differ from the long-term mean by less than 1 mm/yr.

(2) Inclinometers installed in 2020 recorded 20.6–24.9 mm of downslope displacement at the top of the casings between July and November 2022, decreasing gradually with depth to about 20–27 m, whereas the six inclinometers installed in November 2022 recorded 2.8–7.9 mm over 4–12 months, most of it between November 2022 and March 2023. The InSAR results agree with the latter but did not resolve the former. No discrete shear surface was identified within the 30 m casings.

(3) MASW sections show a lower-velocity upper layer (layer averages of 320–596 m/s) corresponding to weathered phyllite, debris and soils, above stiffer phyllite. $V_s$ alone does not establish saturation or strength.

(4) Correlations between SAR-derived reservoir surface area and InSAR displacement were weak ($|r| \leq 0.41$) and not significant after correction for multiple testing; a drawdown control can be neither confirmed nor excluded without reservoir level and piezometric data.

(5) InSAR anomalies were distributed among the susceptibility classes in proportion to their area (frequency ratios 0.92–1.18; chi-square $p \geq 0.81$), so the susceptibility map is not supported by the InSAR data at the available resolution. This result was insensitive to the weights, whereas the class boundaries changed for 4.5–27.2% of the cells under random weight variations.

Open access InSAR can therefore be used at very low cost to exclude fast movements of reservoir slopes over long periods, provided that the moving area is large compared with the resolution of the products (about 100 m) and the movement has an east–west or vertical component, which supports the sustainable management of dams, but at this site it bounds the slope motion only at a few millimetres per year and cannot replace in situ monitoring. The case also shows that the detection threshold and directional sensitivity of InSAR, and the statistical consistency of susceptibility maps with independent observations, should be quantified before such products are used to prioritize monitoring. Future work should include full-resolution InSAR processing or corner reflectors on the slope, reservoir level, piezometric and meteorological records for a quantitative analysis of the hydrological control, a landslide inventory and a high-resolution DEM for a validated susceptibility model, and stability analyses based on laboratory strength parameters.

**Author Contributions:** Conceptualization, T.U.; methodology, T.U.; software, T.U.; validation, T.U.; formal analysis, T.U.; investigation, T.U.; resources, F.K.; data curation, T.U.; writing—original draft preparation, T.U.; writing—review and editing, T.U. and F.K.; visualization, T.U.; supervision, T.U. and F.K. All authors have read and agreed to the published version of the manuscript.

**Funding:** This research received no external funding.

**Institutional Review Board Statement:** Not applicable.

**Informed Consent Statement:** Not applicable.

**Data Availability Statement:** The data presented in this study are available on request from the corresponding author due to third-party data ownership restrictions. The field investigation and monitoring data (MASW, ERT, borehole, and inclinometer data) are not publicly available and require permission from the respective data owners. The Sentinel-1 and Sentinel-2 imagery and SRTM DEM are openly available from the Copernicus Data Space Ecosystem and USGS EarthExplorer, the ESA WorldCover product from https://esa-worldcover.org (accessed on 25 October 2026), and the HydroSHEDS flow accumulation data from https://www.hydrosheds.org (accessed on 25 October 2026). The LiCSAR interferograms are openly available through the COMET-LiCS portal (https://comet.nerc.ac.uk/COMET-LiCS-portal/, accessed on 25 October 2026). The time-series processing scripts are available from the corresponding author on request.

**Acknowledgments:** Sentinel-1 and Sentinel-2 satellite data were provided by the European Space Agency (ESA) through the Copernicus Programme. Digital Elevation Model (DEM) data were obtained from the Shuttle Radar Topography Mission (SRTM). The active fault data used in this study were produced by the General Directorate of Mineral Research and Exploration (MTA). LiCSAR contains modified Copernicus Sentinel data (2017–2024) analysed by the Centre for the Observation and Modelling of Earthquakes, Volcanoes and Tectonics (COMET); LiCSAR uses JASMIN, the UK collaborative data analysis environment. The authors thank the institutions and companies that carried out the site investigation and monitoring of the landslide and made the inclinometer, MASW, ERT and borehole data available.

**Conflicts of Interest:** The authors declare no conflicts of interest.

## Abbreviations

The following abbreviations are used in this manuscript:

| | |
|---|---|
| AHP | Analytic Hierarchy Process |
| COMET | Centre for the Observation and Modelling of Earthquakes, Volcanoes and Tectonics |
| DEM | Digital Elevation Model |
| ERT | Electrical Resistivity Tomography |
| ESA | European Space Agency |
| FR | Frequency ratio |
| GACOS | Generic Atmospheric Correction Online Service |
| GIS | Geographic Information System |
| HPP | Hydroelectric Power Plant |
| InSAR | Interferometric Synthetic Aperture Radar |
| IW | Interferometric Wide swath |
| LiCSAR | Looking into Continents from Space with Synthetic Aperture Radar |
| LiCSBAS | LiCSAR Small Baseline Subset time-series package |
| LOS | Line-of-Sight |
| MASW | Multichannel Analysis of Surface Waves |
| MTA | General Directorate of Mineral Research and Exploration |
| NDVI | Normalized Difference Vegetation Index |
| NSBAS | New Small Baseline Subset |
| SAR | Synthetic Aperture Radar |
| SRTM | Shuttle Radar Topography Mission |
| TWI | Topographic Wetness Index |
| VV | Vertical transmit, vertical receive polarization |

## References

1. Cavuslu, M.; Inyurt, S. Determination of future creep and seismic behaviors of dams using 3D analyses validated by long-term levelling measurements. *J. Civ. Struct. Health Monit.* **2024**, *14*, 1505–1532. [CrossRef]
2. ICOLD. *Dam Surveillance Guide*, 1st ed.; CRC Press: Boca Raton, FL, USA, 2018. [CrossRef]

3. Schuster, R.L.; Highland, L.M. *Socioeconomic and Environmental Impacts of Landslides in the Western Hemisphere*; Open-File Report 01-276; U.S. Geological Survey: Reston, VA, USA, 2001. [CrossRef]
4. Ebrahim, K.M.P.; Gomaa, S.M.M.H.; Zayed, T.; Alfalah, G. Recent phenomenal and investigational subsurface landslide monitoring techniques: A mixed review. *Remote Sens.* **2024**, *16*, 385. [CrossRef]
5. Ruiz-Armenteros, A.M.; Marchamalo-Sacristán, M.; Lamas-Fernández, F.; Hernández-Cabezudo, Á.; Fernández-Landa, A.; Delgado-Blasco, J.M.; Bakon, M.; Lazecky, M.; Perissin, D.; Papco, J.; et al. Integrated monitoring of dams and large ponds: The role of satellite radar interferometry and the European ground motion service. *Appl. Geomat.* **2025**, *17*, 379–392. [CrossRef]
6. Ruiz-Armenteros, A.M.; Marchamalo-Sacristán, M.; Lamas-Fernández, F.; Delgado-Blasco, J.M.; Jurado-Rodríguez, J.M.; Jurado-Rodríguez, D.; Bakon, M.; Lazecky, M.; Perissin, D.; Papco, J.; et al. Routine monitoring of hydraulic infrastructures using the European Ground Motion Service and other satellite radar sensors. *Procedia Comput. Sci.* **2024**, *239*, 2308–2315. [CrossRef]
7. Salyamova, K.; An, E.; Nishonov, N.; Toshmatov, K.; Turdikulov, K. Long-term monitoring of earth dam of the Charvak hydroelectric power plant (HPP) considering the water level of the reservoir. *E3S Web Conf.* **2023**, *462*, 02050. [CrossRef]
8. Ziemer, J.; Jänichen, J.; Stein, G.; Liedel, N.; Wicker, C.; Last, K.; Denzler, J.; Schmullius, C.; Shadaydeh, M.; Dubois, C. Identifying deformation drivers in dam segments using combined X- and C-band PS time series. *Remote Sens.* **2025**, *17*, 2629. [CrossRef]
9. Milillo, P.; Bürgmann, R.; Lundgren, P.; Salzer, J.; Perissin, D.; Fielding, E.; Biondi, F.; Milillo, G. Space geodetic monitoring of engineered structures: The ongoing destabilization of the Mosul dam, Iraq. *Sci. Rep.* **2016**, *6*, 37408. [CrossRef] [PubMed]
10. Ghorbani, Z.; Khosravi, A.; Maghsoudi, Y.; Vroman, E.; Stanton, S. InSAR-based deformation monitoring of levee systems: From regional context to local stability. *SSRN* **2025**. *preprint*. [CrossRef]
11. Liu, H.; Zhao, W.; Qin, Z.; Wang, T.; Li, G.; Zhu, M. Time-series InSAR deformation monitoring of high fill characteristic canal of South–North Water Diversion Project in China. *Appl. Sci.* **2023**, *13*, 6415. [CrossRef]
12. Ghadimi, M.; Kiani, M. Deformation risk assessment of the Lar Dam: Monitoring its stability condition. *Sustainability* **2024**, *16*, 4335. [CrossRef]
13. Azadi, A.; Esmatkhah Irani, A.; Azarafza, M.; Hajialilue Bonab, M.; Behrooz Sarand, F.; Derakhshani, R. Coupled numerical and analytical stability analysis charts for an earth-fill dam under rapid drawdown conditions. *Appl. Sci.* **2022**, *12*, 4550. [CrossRef]
14. Gao, Y.; Zhu, D.; Zhang, F.; Lei, G.H.; Qin, H. Stability analysis of three-dimensional slopes under water drawdown conditions. *Can. Geotech. J.* **2014**, *51*, 1355–1364. [CrossRef]
15. Zhu, D.; Griffiths, D.V.; Fenton, G.A.; Huang, J.; Gao, Y. Reliability analysis of slopes under slow drawdown conditions. *Géotechnique* **2026**, *76*, 835–841. [CrossRef]
16. Wu, W.; Liu, G.; Hu, J.; Liu, L.; Sun, Q. Investigating deformation mechanism of earth-rock dams with InSAR and numerical simulation: Application to Liuduzhai Reservoir Dam, China. *Remote Sens.* **2023**, *15*, 4110. [CrossRef]
17. Cheng, Y.; Pang, H.; Li, Y.; Fan, L.; Wei, S.; Yuan, Z.; Fang, Y. Applications and advancements of spaceborne InSAR in landslide monitoring and susceptibility mapping: A systematic review. *Remote Sens.* **2025**, *17*, 999. [CrossRef]
18. Ruiz-Armenteros, A.M.; Marchamalo-Sacristán, M.; Bakoň, M.; Lamas-Fernández, F.; Delgado, J.M.; Sánchez-Ballesteros, V.; Papco, J.; González-Rodrigo, B.; Lazecky, M.; Perissin, D.; et al. Monitoring of an embankment dam in southern Spain based on Sentinel-1 time-series InSAR. *Procedia Comput. Sci.* **2021**, *181*, 353–359. [CrossRef]
19. Liu, S.; Segoni, S.; Raspini, F.; Yin, K.; Zhou, C.; Zhang, Y.; Casagli, N. Satellite InSAR as a new tool for the verification of landslide engineering remedial works at the regional scale: A case study in the Three Gorges Reservoir Area, China. *Appl. Sci.* **2020**, *10*, 6435. [CrossRef]
20. Salyamova, K.; Tashmatov, K.; Nishonov, N.; An, E. Comparing static analysis of earth dam strength with space monitoring data. *E3S Web Conf.* **2025**, *623*, 02010. [CrossRef]
21. Wang, K.-L.; Lin, J.-T.; Chu, H.-K.; Chen, C.-W.; Lu, C.-H.; Wang, J.-Y.; Lin, H.-H.; Chi, C.-C. High-resolution LiDAR digital elevation model referenced landslide slide observation with differential interferometric radar, GNSS, and underground measurements. *Appl. Sci.* **2021**, *11*, 11389. [CrossRef]
22. Ouyang, Y.; Feng, T.; Feng, H.; Wang, X.; Zhang, H.; Zhou, X. Deformation monitoring and potential risk detection of in-construction dams utilizing SBAS-InSAR technology—A case study on the Datengxia Water Conservancy Hub. *Water* **2024**, *16*, 1025. [CrossRef]
23. Maltese, A.; Pipitone, C.; Dardanelli, G.; Capodici, F.; Muller, J.-P. Toward a comprehensive dam monitoring: On-site and remote-retrieved forcing factors and resulting displacements (GNSS and PS–InSAR). *Remote Sens.* **2021**, *13*, 1543. [CrossRef]
24. Ciampi, P.; Mangifesta, M.; Giannini, L.M.; Esposito, C.; Scalella, G.; Burchini, B.; Sciarra, N. Geophysical and remote sensing techniques for large-volume and complex landslide assessment. *Remote Sens.* **2025**, *17*, 2029. [CrossRef]
25. Dini, B.; Manconi, A.; Loew, S.; Chophel, J. The Punatsangchhu-I dam landslide illuminated by InSAR multitemporal analyses. *Sci. Rep.* **2020**, *10*, 8304. [CrossRef] [PubMed]
26. Li, J.T.; Xu, H.P.; Shan, L.; Liu, W.; Chen, G.Z. An efficient compressive sensing based PS-DInSAR method for surface deformation estimation. *Meas. Sci. Technol.* **2016**, *27*, 114001. [CrossRef]

27. Galloway, D.L.; Hoffmann, J. The application of satellite differential SAR interferometry-derived ground displacements in hydrogeology. *Hydrogeol. J.* **2007**, *15*, 133–154. [CrossRef]
28. Massonnet, D.; Feigl, K.L. Radar interferometry and its application to changes in the Earth's surface. *Rev. Geophys.* **1998**, *36*, 441–500. [CrossRef]
29. Hu, Z.; Mallorquí, J.J. An accurate method to correct atmospheric phase delay for InSAR with the ERA5 global atmospheric model. *Remote Sens.* **2019**, *11*, 1969. [CrossRef]
30. Bekaert, D.P.S.; Walters, R.J.; Wright, T.J.; Hooper, A.J.; Parker, D.J. Statistical comparison of InSAR tropospheric correction techniques. *Remote Sens. Environ.* **2015**, *170*, 40–47. [CrossRef]
31. Lazecký, M.; Spaans, K.; González, P.J.; Maghsoudi, Y.; Morishita, Y.; Albino, F.; Elliott, J.; Greenall, N.; Hatton, E.; Hooper, A.; et al. LiCSAR: An automatic InSAR tool for measuring and monitoring tectonic and volcanic activity. *Remote Sens.* **2020**, *12*, 2430. [CrossRef]
32. Morishita, Y.; Lazecky, M.; Wright, T.; Weiss, J.; Elliott, J.; Hooper, A. LiCSBAS: An open-source InSAR time series analysis package integrated with the LiCSAR automated Sentinel-1 InSAR processor. *Remote Sens.* **2020**, *12*, 424. [CrossRef]
33. Doin, M.-P.; Lasserre, C.; Peltzer, G.; Cavalié, O.; Doubre, C. Corrections of stratified tropospheric delays in SAR interferometry: Validation with global atmospheric models. *J. Appl. Geophys.* **2009**, *69*, 35–50. [CrossRef]
34. Berardino, P.; Fornaro, G.; Lanari, R.; Sansosti, E. A new algorithm for surface deformation monitoring based on small baseline differential SAR interferograms. *IEEE Trans. Geosci. Remote Sens.* **2002**, *40*, 2375–2383. [CrossRef]
35. López-Quiroz, P.; Doin, M.-P.; Tupin, F.; Briole, P.; Nicolas, J.-M. Time series analysis of Mexico City subsidence constrained by radar interferometry. *J. Appl. Geophys.* **2009**, *69*, 1–15. [CrossRef]
36. Buono, A.; Nunziata, F.; de Macedo, C.R.; Velotto, D.; Migliaccio, M. A sensitivity analysis of the standard deviation of the copolarized phase difference for sea oil slick observation. *IEEE Trans. Geosci. Remote Sens.* **2019**, *57*, 2022–2030. [CrossRef]
37. Gao, M.; Dong, W.; Chen, L.; Wu, Z. Automatic extraction of water body from SAR images considering enhanced feature fusion and noise suppression. *Appl. Sci.* **2025**, *15*, 2366. [CrossRef]
38. Tan, J.; Tang, Y.; Liu, B.; Zhao, G.; Mu, Y.; Sun, M.; Wang, B. A self-adaptive thresholding approach for automatic water extraction using Sentinel-1 SAR imagery based on OTSU algorithm and distance block. *Remote Sens.* **2023**, *15*, 2690. [CrossRef]
39. Abdelrahman, K.; Alarifi, S.S. Subsurface geological characteristics of Al-Ammariah area, Saudi Arabia, for sustainable urban development using multichannel analysis of surface waves. *Sci. Rep.* **2025**, *15*, 35687. [CrossRef] [PubMed]
40. Leonardi, G.; Palamara, R.; Manti, F.; Tufano, A. GIS-multicriteria analysis using AHP to evaluate the landslide risk in road lifelines. *Appl. Sci.* **2022**, *12*, 4707. [CrossRef]
41. Senouci, R.; Taibi, N.-E.; Teodoro, A.C.; Duarte, L.; Mansour, H.; Yahia Meddah, R. GIS-based expert knowledge for landslide susceptibility mapping (LSM): Case of Mostaganem coast district, west of Algeria. *Sustainability* **2021**, *13*, 630. [CrossRef]
42. Zhou, J.; Tan, S.; Li, J.; Xu, J.; Wang, C.; Ye, H. Landslide susceptibility assessment using the analytic hierarchy process (AHP): A case study of a construction site for photovoltaic power generation in Yunxian County, Southwest China. *Sustainability* **2023**, *15*, 5281. [CrossRef]
43. Jiang, H.; Zhang, C.-H.; Zhou, Y.-D.; Pan, J.-W.; Wang, J.-T.; Wu, M.-X.; Fan, Q.-X. Mechanism for large-scale canyon deformations due to filling of large reservoir of hydropower project. *Sci. Rep.* **2020**, *10*, 12155. [CrossRef] [PubMed]
44. Tong, L.H.; Wu, B.N.; Lei, Z.X.; Xu, C.J. Unified creeping model identifying the critical state of granular materials. *J. Appl. Phys.* **2022**, *132*, 055105. [CrossRef]
45. Tong, L.; Fu, L.; Xu, C.; Ding, H.; Xiao, M. Loading rate effect on the strength of granular material considering particle rotation. *Comput. Geotech.* **2023**, *162*, 105680. [CrossRef]
46. Hu, Z.; Wei, H.; Yu, L. Slip instability mechanisms of filled faults under unloading: Comparisons between planar and undulating interfaces at two unloading rates. *Eng. Fract. Mech.* **2026**, *347*, 112688. [CrossRef]
47. Wu, G.; Tan, Y.; Xu, Z.; Yuan, Z.; Zhang, J.; He, Y.; Wang, C. XAI-aided method for accurately assessing the stability of unlined double tunnels in rock masses. *Transp. Geotech.* **2026**, *61*, 102052. [CrossRef]
48. Lehner, B.; Verdin, K.; Jarvis, A. New global hydrography derived from spaceborne elevation data. *Eos Trans. AGU* **2008**, *89*, 93–94. [CrossRef]
49. He, Y.; Duan, Z.-L.; Ding, X.-H.; Zhang, Z.; Mayoulou, R.E.; Zhu, K.-F. Spatiotemporal prediction for groundwater heavy metal contamination using Soft-DTW-based clustering and graph neural network framework. *Water Res.* **2026**, *291*, 125245. [CrossRef] [PubMed]


**Disclaimer/Publisher's Note:** The statements, opinions and data contained in all publications are solely those of the individual author(s) and contributor(s) and not of MDPI and/or the editor(s). MDPI and/or the editor(s) disclaim responsibility for any injury to people or property resulting from any ideas, methods, instructions or products referred to in the content.